GRAIN SIZE DEPENDENCE OF TWIN-DOMINANT DEFORMATION IN ROLLED MAGNESIUM AZ31 INVESTIGATED BY IN SITU MICROSCOPIC IMAGE CORRELATION

by

Sevinç Uçar

B.S, Mechanical Engineering, Bilkent University, 2014

Submitted to the Institute for Graduate Studies in
Science and Engineering in partial fulfillment of
the requirements for the degree of
Master of Science

Graduate Program in Mechanical Engineering

Boğaziçi University

2017

ACKNOWLEDGEMENTS

I would like to thank to my family for their support and encouragement. No matter how far we are, I always felt their unconditional love and trust in me, throughout my educational life.

I am grateful to my thesis advisor Assoc. Prof. C. Can Aydıner for his guidance, support and patience.

I would also like to thank to the members of the committee Assist. Prof. Mert Efe and Assist. Prof. Özgün Konca for their remarks and suggestion to improve my study.

I am very thankful to my lab mates Nima Shafaghi, Enver Kapan, Olcay Türkoğlu, Buğra Üçel, Mona Raeissi, and Necdet Özdur for their help and friendship. Throughout my study in Boğaziçi University, Mechanics of Advanced Materials Lab, aka KB243 became a second home for me, thanks to them.

I also would like to thank to my dearest friend Esen Yel who understands me without speaking a word, and have supported me in making the hardest decisions of my life.

This work was in part supported by the Scientific and Technological Research Council of Turkey (TUBITAK), Grant No: 114M215.

ABSTRACT

GRAIN SIZE DEPENDENCE OF TWIN-DOMINANT DEFORMATION IN ROLLED MAGNESIUM AZ31 INVESTIGATED BY IN SITU MICROSCOPIC IMAGE CORRELATION

In this study, twin-dominant deformation in rolled Magnesium AZ31 is explored with multi-scale in situ digital image correlation (DIC) by parametrizing grain size. Two samples extracted along the rolling direction are used for the grain size comparison: i) fine-grained (FG) sample with ~11 μm, ii) coarse-grained (CG) sample with ~25 μm grain size. The samples are tested under compressive loading that activates the tensile twinning system $\{10\bar{1}2\}\langle\bar{1}011\rangle$. Sample surfaces are monitored with macroscopic and microscopic imaging as load is incremented in position control. By area scanning the sample under microscopic optics, macroscopic deformation structures are mapped with microscopic resolution. These ultra-high-resolution maps are used to compare strain distributions of FG and CG samples. In terms of stress response and the distribution of deformation patterns, the effect of grain size is noticeable. The level of stress that FG sample exhibits on the twin plateau (flat section of the stress strain curve) is higher than that of the CG sample (80 and 60 MPa, respectively). Both samples display heterogeneous deformation in the form of ±45° inclined bands. Quantitative analysis of the deformed regions shows that average strains in deformation bands are always higher in FG sample than in CG sample but by a small margin (~10%). The nominal average standalone band strain in the axial direction spans from 1.5 to 2 % to be put in perspective of the 6.5% twin transformation strain. A quantity named sole-twin-activity volume fraction , V_{STA}, is defined over the bands that presumes entire strain accomodation comes from tensile twinning, V_{STA} is slightly higher in FG sample compared to the CG sample by the same ~10% margin. V_{STA} remains constant on a singular band even when it expands, confirming the conjecture that band strain and corresponding V_{STA} are characteristic values. Only when bands intersect and interact, the strain in these localization structures rise noticeably.

ÖZET

TANECİK BÜYÜKLÜĞÜNE BAĞIMLILIĞININ İKİZLENEN HADDELENMİŞ MAGNEZYUM AZ31 ÜZERİNDE *YERİNDE* İMGE KORELASYONU İLE İNCELENMESİ

İkizlenen Magnezyum AZ31 alaşımının tanecik büyüklüğüne bağımlı deformasyonu, çok ölçekli yerinde dijital imge korelasyonu ile araştırılmıştır. Tanecik büyüklüğü karşılaştırması için 2 adet haddelenmiş numune kullanılmıştır. Tanecik boyutları: i) küçük taneli (KT), ~11 μm ii) büyük taneli (BT), ~25 μm. Numuneler, $\{10\bar{1}2\}\langle\bar{1}011\rangle$ ikizlenme sistemini harekete geçirecek şekilde basılarak yüklenmiştir. İkizlenen malzemenin deformasyon davranışları, deneyler sırasında numuneler makroskobik ve mikroskobik ölçeklerde izlenmiştir. Deformasyon haritaları, KT ve BT numunelerin yüzeylerindeki gerinim dağılımlarını karşılaştırmak için kullanılmıştır. Bunlara göre, gerilme tepkisi ve deformasyon dağılımı bakımından tanecik büyüklüğünün açıkça görülebilir etkileri vardır: KT numunedeki ikizlenme platosu gerilmesinin BT numuneninkinden yüksek olduğu görülmüştür (80 ve 60 MPa). Her iki numune de yükleme yönüne ±45°'de konumlanan deformasyon bantları ile heterojen deformasyon sergilemiştir ancak bantlar, KT numunede dağınık ve birbiriyle kesişen çapraz bant yapılarına sahipken, BT numunede tek yönlü ve lokalize durumdadırlar. Deforme olmuş bölgelerin sayısal olarak analizi yapıldığında ise KT numune üzerindeki ortalama gerinimin BT numunedekinden deney boyunca daha yüksek olduğu (~10% oranında), ancak değerlerinin birbirine yakın olduğu görülmüştür. Başka bir deforme olmuş bölgeyle kesişmeyen ve etkileşime girmeyen bantların çekme yönündeki ortalama gerinimleri %1.5-2 arasında değişmektedir. Bir bant üzerindeki bütün gerinimin ikizlenmeden kaynaklandığı farz edilerek, sadece-ikizlenme-bazlı hacim oranı, V_{STA}, adında bir nicelik tanımlanmıştır. KT numunedeki V_{STA}, BT numunedekinden yaklaşık %10 daha yüksek olmakla birlikte değerleri oldukça yakındır. Tekil bantların genişlikleri arttığında dahiV_{STA} değerlerinin bantlar sabit kalması, V_{STA} 'nın karakteristik değeri olduğu varsayımını doğrulamaktadır. Sadece deformasyon bantları etkileşime girdiği takdirde, kesişim bölgelerinde yoğunlaşan bir gerinim artışına rastlanmıştır.

TABLE OF CONTENTS

ACKNOWLEDGEMENTS iii

ABSTRACT iv

ÖZET v

LIST OF FIGURES ix

LIST OF TABLES xii

LIST OF SYMBOLS xiii

LIST OF ACRONYMS/ABBREVIATIONS xiv

1. INTRODUCTION 1

1.1. Motivation 1

1.2. Background 3

1.2.1. Deformation Mechanisms of Magnesium 3

1.2.2. Deformation Twinning 4

1.2.3. Factors on The Mechanical Behavior of Polycrystalline Aggregate 5

1.2.3.1. Preferred Orientation (Texture). 5

1.2.3.2. Grain Size 6

1.2.4. Twin volume fraction 7

1.3. Scope 8

2. EXPERIMENT 10

2.1. Sample Preparation 10

2.1.1. Material Properties 10

2.1.2. Sample Geometry 10

2.1.3. Surface Preparation 11

2.1.3.1. Metallography. 11

2.1.3.2. Speckle pattern application. 12

2.2. Experimental Setup 12

2.2.1. Setup 12

2.2.2. DIC Application 13

2.2.3. Test Procedure 16

3. RESULTS 18

3.1. Overall Mechanical Behavior 18

3.2. Analysis of Full-field Strain Maps 19

3.2.1. Strain Localization Patterns 19

3.2.2. Statistical Analysis of Localization Bands 21

3.2.3. In-plane Poisson’s ratio over shear band structures 30

4. DISCUSSION 32

4.1. Filtering Strain Data 34

5. CONCLUSION 39

6. FUTURE WORK 41

REFERENCES 42

APPENDIX A: POLE FIGURES 47

LIST OF FIGURES

Figure 1.1. Slip and twinning systems of Magnesium…….. 3

Figure 1.2. $\{10\bar{1}2\}\langle\bar{1}011\rangle$Twinning HCP crystal……..…… 4

Figure 1.3. Rolling Process – Preferred Orientation Of Hcp Crystals…….. 5

Figure 1.4. Extrusion Process – Preferred Orientation Of Hcp Crystals……... 6

Figure 2.1. Pole Figure of Rolled Material……..... 10

Figure 2.1. Sample Dimensions…… 11

Figure 2.2. Sample Dimensions…… 11

Figure 2.3. Observation surface is on RD plane (RD: rolling direction, ND: normal direction, TD: transverse direction) ……..… 11

Figure 2.4. Speckle Pattern before (a) and after (b) painting……..... 12

Figure 2.5. Experimental setup: (a) macro-DIC optics, (b) micro-DIC optics, (c) positioning stages, (d) micro tensile/compression loading module, (e) controller of the loading module, (f) strain gage data acquisition module, (g) computers, (h) Aluminum frame……... 13

Figure 2.6. Elements of the setup about the loading stage (a) Sample, (b) LVDT transducer, (c) power screws, (d) grips, (e) mirror…… 14

Figure 2.7. Grid structure of (a) a macro-DIC image, (b) micro-DIC image (~35000

points)……...…… 15

Figure 3.1. Stress-strain curves for both fine grained (FG) and coarse grained (CG) samples under uniaxial compression……..... 18

Figure 3.2. Macro DIC strain maps of FG sample at $\varepsilon_M =$ (a) -0.16%, (b) -0.27%, (c) -0.39%, (d) -0.6%, (e) -0.78%, (f) -1.42% (g) -1.61% (h) -1.69% (i) -2.01% (j) -2.16%..... 19

Figure 3.3. Macro DIC strain maps of CG sample at $\varepsilon_M =$ (a) -0.14%, (b) -0.3 %, (c) -0.43%, (d) -0.85%, (e) -1.06%, (f) -1.24%, (g) -1.55%, (h) -1.71% (i) -1.84% (j) -2.08%..... 20

Figure 3.4. Macro and micro DIC strain maps of FG sample at $\varepsilon_M =$ (a) -0.16%, (b) -0.6%, (c) -0.78%, (d) -1.42%, (e) -2.16%..... 21

Figure 3.5. Macro and micro DIC strain maps of CG sample at $\varepsilon_M =$ (a) -0.3%, (b) -0.43%, (c) -0.85%, (d) -1.24%, (e) -2.08%..... 22

Figure 3.6. Masked deformation bands and the histograms of masked regions of FG sample at $\varepsilon_M =$ (a) -0.6%, (b) -0.78%..... 23

Figure 3.7. Masked deformation bands and the histograms of masked regions of CG sample at $\varepsilon_M =$ (a) -0.43%, (b) -0.85%..... 24

Figure 3.8. Masked deformation bands and the histograms of masked regions of FG sample at $\varepsilon_M =$ (a) -1.42%, (b) -2.16% …… 25

Figure 3.9. Masked deformation bands and the histograms of masked regions of CG sample at $\varepsilon_M =$ (a) -1.24%, (b) -2.08% …… 25

Figure 3.10. Masked cross regions and histograms for FG sample at $\varepsilon_M =$ -0.6%..... 28

Figure 3.11. Masked cross regions and histograms for FG sample at ε_M = -0.78%..... 29

Figure 3.12. Masked cross regions and histograms for FG sample at ε_M = -1.42%..... 29

Figure 4.1. Sole-twin-activity volume fraction, V_{STA}, vs. absolute macroscopic strain, ε_M for both fine-grained (FG) and coarse-grained (CG) samples... 34

Figure 4.2. (a) Masked and filtered($\varepsilon_{yy}^{lim} > 3\%$) deformation band of CG sample at ε_M = 0.43%; (b) blow-up of filtered domains shown inside yellow boundaries; (c) histogram of the filtered strain data…… 35

Figure 4.3. Fraction (*V*) of the number of filtered strain data points, ($\varepsilon_{yy} > \varepsilon_{yy}^{lim}$), to the number of the entire strain data plotted against ε_{yy}^{lim} for CG sample within the masked band (blue curve) and all sample surface (green curve) at ε_M = 0.43%..... 36

Figure 4.4. Fraction (*V*) of the number of filtered strain data points, ($\varepsilon_{yy} > \varepsilon_{yy}^{lim}$), to the number of the entire strain data plotted against ε_{yy}^{lim} for FG (a) and CG (b) at different load points……. 37

Figure A.1. Pole Figures of FG and CG materials obtained from a Bruker D8 Discover X-Ray Diffraction System……... 47

LIST OF TABLES

Table 3 1. Average micro-DIC normal strains in y-direction, ε_{yy} (%), in x-direction, ε_{xx} (%); standard deviation of the axial micro-DIC strain distribution, ε_{yy}^{std}, and Poisson's ratio, ν_{xy}, defined over individual masked bands of FG sample (bands in Fig. 3.6 and Fig. 3.8) at various stages of loading specified by sample strain, ε_M…….……. 27

Table 3.2. Average micro-DIC normal strains in y-direction, ε_{yy} (%), in x-direction, ε_{xx} (%); standard deviation of the axial micro-DIC strain distribution, ε_{yy}^{std}, and Poisson's ratio, ν_{xy}, defined over individual masked bands of CG sample (bands in Fig. 3.7 and Fig. 3.9) at various stages of loading specified by sample strain, ε_M…… 27

Table 3.3. Average micro-DIC normal strains in y-direction, ε_{yy} (%), in x-direction, ε_{xx} (%); standard deviation of the axial micro-DIC strain distribution, ε_{yy}^{std}, and Poisson's ratio, ν_{xy}, defined over band intersections in the FG sample (Figs. 3.10-12, a-c) at various stages of loading specified by sample strain, ε_M…….....…….. 30

LIST OF SYMBOLS

a, c	lattice parameters of HCP unit cell
u	displacement along x-axis
v	displacement along y-axis
V_{STA}	sole-twin-activity volume fraction
V	fraction of the number of filtered strain data points to the number of the entire strain data
σ	stress
ε	infinitesimal strain
ω	infinitesimal rotation
ε_M	average macro-DIC strain in *y*-direction
ε_{xx}	micro-DIC strain in x-direction
ε_{yy}	micro-DIC strain in *y*-direction
ε_{zz}	micro-DIC strain in z-direction
$\bar{\varepsilon}_{xx}$	average micro-DIC strain in *x*-direction
$\bar{\varepsilon}_{yy}$	average micro-DIC strain in *y*-direction
ε_{yy}^{lim}	limit value for filtering strain data
ν_{yx}	Poisson's ratio on *xy*-plane

LIST OF ACRONYMS/ABBREVIATIONS

2D	Two dimensional
CDF	Cumulative distribution function
DIC	Digital image correlation
EBSD	Electron back-scattering diffraction
ED	Extrusion direction
EDM	Electrical discharge machining
HCP	Hexagonal close-packed
ND	Normal
NDf	Neutron diffraction
PDF	Probability distribution function
RD	Rolling direction on a rolled plate
TD	Transverse direction on a rolled plate

1. INTRODUCTION

1.1. Motivation

Magnesium alloys are suitable materials for structural applications in aerospace and automotive because of their high strength to weight ratio. However, their ductility is limited at room temperature. This leads to failure at lower strains and poor formability at room temperature. Hexagonal close-packed (HCP) crystals have a low-symmetry structure with a single close-packed plane, the basal plane. The easy slip systems (basal or prism) operate along the close-packed directions <a> and thus they cannot accommodate c-axis strains. In Magnesium alloys, c-axis elongation is primarily provided by deformation twinning. Twin mechanisms have a more complex nature than dislocation slip: They reorient a part of a crystal and has a unipolar nature. Unipolar activation means that if the twin is activated along one loading path; it will not be activated along the reverse path. In textured polycrystalline aggregates of Magnesium, this leads to the well-known tension-compression anisotropy. [1–4]. Microstructurally, twin transformation causes abrupt strain localization in the crystals favorably oriented for twinning. Thus, complex and anisotropic plastic mechanisms of this material lead to strain heterogeneity. Localized deformation, in turn leads to damage and failure, which are both local phenomena [5, 6]**.** For predicting failure and plasticity processes in Magnesium alloys, it is significant to understand twinning mechanisms and their connection to strain localization.

Yield strength of a material typically increases while grain size decreases (Hall-Petch effect [7-9]). Macroscopically, mechanical response of twin dominant deformation also depends on the average grain size in a similar manner. At the crystallite scale, the nature of twin formation and growth changes with grain size. Further, particularly tensile twinning is a propagating defect in Magnesium alloys. Twin formation in one grain precipitates twin formation in the next grain, broadly called “twin transmission”. In terms of twin transmission, it is reported that collaborative twin nucleation activity increases as the grain size is reduced [10–16]. These studies use various methods to experimentally investigate the effect of grain size such as neutron diffraction (NDf), electron backscatter diffraction

(EBSD) and acoustic emission (AE). Though EBSD is a powerful method for both representing grain structure and orientations spatially, it has a limited statistical significance mostly. NDf on the contrary, provide large amount of volumetric data but lacks morphological evidence. Although AE is a suitable method to detect twin nucleation, it cannot acquire the twin growth signals. Therefore, it is only utilized as a supplementary method.

To experimentally investigate the strain heterogeneity originated by twinning, monitor the material morphology, and provide a high statistical significance at the same time, strain mapping techniques are utilized such as digital image correlation (DIC). The method involves comparison of two images (undeformed and deformed) numerically. The theory and application of DIC is explained by [17] in detail. DIC has no inherent length scale and its microscopic implementation has been recently used to investigate strain heterogeneity in many materials. Efstathiou *et al.*(2010) uses multi-scale *ex situ* DIC to reveal the strain heterogeneity in Hadfield steel and random-textured HCP Titanium [18, 19].

For Magnesium AZ31, Hazeli *et al.* (2013) [11] presents the effect of loading orientation on formation of twinning and deformation heterogeneity as a result of macroscopic DIC. A more detailed macro-scale *in situ* DIC study of Kapan *et al.* (2017) [20] provides an analysis of texture dependence of deformation localization in the same alloy. Multi-scale full-field DIC study of Aydıner and Telemez (2014) [21] focuses on shear band formations during the intense twinning in rolled Mg AZ31. In DIC studies that target this material, the effect of grain size on the strain localization behavior has not been explored systematically.

In this study, grain size dependent strain heterogeneity of rolled Mg AZ31 is investigated by multi-scale, in-situ DIC experiments. For that purpose, two samples, one fine-grained (FG) and the other coarse-grained (CG), are compressed and sample surfaces are monitored at macroscopic and microscopic scales. Through scanning, macroscopic deformation structures are mapped at microscopic resolution. Then, microstructural distribution of strain, with particular emphasis inside the deformation bands, is statistically analyzed to compare the strain heterogeneity characteristics of FG and CG samples.

1.2. Background

1.2.1. Deformation Mechanisms of Magnesium

Plastic deformation is typically carried by dislocation slip in a crystal. Slip tends to occur on the planes with maximum atomic density and in the directions with closest atomic distance. Requiring the minimum amount of resolved shear stress to be activated, these are referred to as the slip systems of a material. A crystalline material must have five independent slip systems to be ductile, i.e., undergo an arbitrary strain state. In the case of insufficient number of independent slip systems, another deformation mechanism must contribute to plastic deformation if the material is to remain ductile [7, 22].

Hexagonal close-packed (HCP) Mg alloys have on paper more than five independent slip systems albeit with very different activation ease, namely, two basal (easy) slip systems $\{00.2\}\langle 11.0\rangle$ (Figure 1.1b), two prismatic $\{10.0\}\langle 11.0\rangle$ slip systems (Figure 1.1b), two pyramidal slip systems $\{10.1\}\langle 11.0\rangle$ and six <c+a> pyramidal $\{11.2\}\langle 11.3\rangle$ (Figure 1.1c and Figure 1.1d). At room temperature, these slip systems cannot be activated by uniaxial load along the c-axis since <c+a> pyramidal slip is the only mode whose direction has a component along the c-axis and its operation requires very high temperatures [23]. Therefore, another deformation mechanism is required for the ductility of a Mg alloy at room temperature in case of straining parallel to c-axis, which is called twinning.

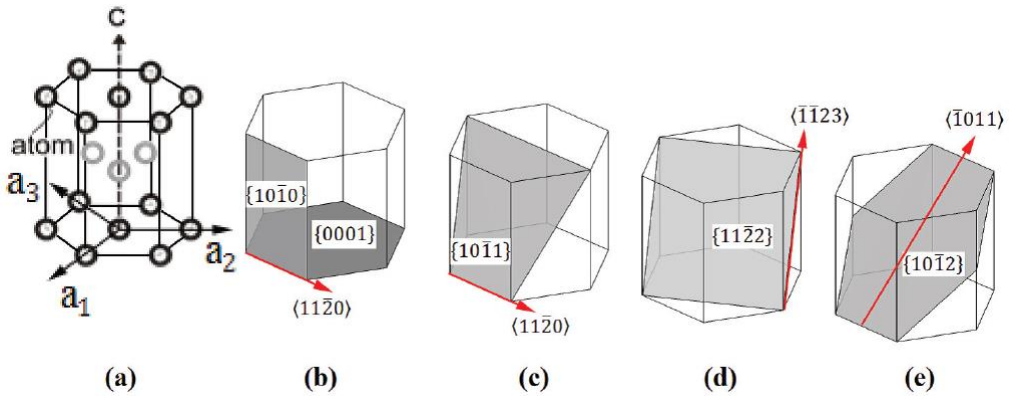

Figure 1.1. Slip and twinning systems of Magnesium

1.2.2. Deformation Twinning

Deformation twinning is reorientation of a group of atoms within a crystal so that the reoriented region becomes a "mirror image" of the remaining untwinned region, separated by the twin plane. This sudden process is called twin nucleation. [24]. Expansion of the reoriented structure with shearing between parallel planes and producing a twin band in the crystal is called twin growth. The critical resolved shear stress required for twin nucleation is larger than that is required for the twin growth [22].

Twinning is a unidirectional mechanism. This means, the critical resolved shear stress that initiates twinning does not operate in the reversal direction. Activation of twinning depends on the lattice parameters. The most common twinning mechanism is $\{10\bar{1}2\}\langle\bar{1}011\rangle$ tensile twinning system (Figure 1.1e) for the HCP metals. $\{10\bar{1}2\}\langle\bar{1}011\rangle$ is initiated by tension when the axial ratio c/a is lower than 1.732. For Mg Alloys, the axial ratio $c/a = 1.624$. Activation of $\{10\bar{1}2\}\langle\bar{1}011\rangle$ tensile twinning reorients c-axes with angle of $86.6°$ and 13% characteristic shear strain for mechanism. It is heavily activated by c-axis tension at lower strain values and room temperature especially for load-texture combinations at which basal slip cannot be activated [22, 25].

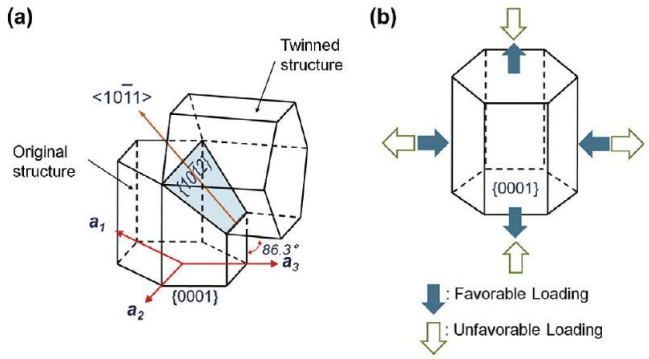

Figure 1.2. $\{10\bar{1}2\}\langle\bar{1}011\rangle$ Twinning HCP crystal (reproduced from Kim *et al*, 2010 [26])

1.2.3. Factors on The Mechanical Behavior of Polycrystalline Aggregate

Preferred Orientation (Texture). Crystallographic orientation distribution (texture) of a polycrystalline material is typically determined by manufacturing processes that the material endures. These processes orient the crystals in a preferred direction, causing texture formation. For wrought Magnesium, the texture induced by the two major forming processes is different: Rolling process results in strong basal pole component parallel to the normal direction (ND) of a Mg plate (see Figure 1.3). On the other hand, extrusion produces a texture such that c-axes of the preferred orientations are perpendicular to the extrusion direction (ED) but randomly distributed about it (see Figure 1.4) [22]. When compression is applied perpendicular to ND of the plate, governing deformation mechanism becomes tensile twinning. Compression of an extruded material parallel to the ED also leads to a tensile-twin dominant deformation. If the load is applied in a different configuration, elastic and plastic properties change, and twinning mechanism may not be activated at lower strains.

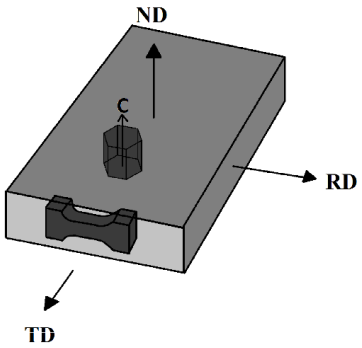

Figure 1.3. Rolling Process – Preferred Orientation Of Hcp Crystals

In case of plastic deformation controlled by $\{10\bar{1}2\}\langle\bar{1}011\rangle$ tensile twin, rolled and extruded materials display distinct deformation behavior in terms of strain heterogeneity. Kapan *et al.* (2017) [20] shows that extruded sample exhibits relatively homogeneous deformation patterns on the sample surface whereas strain is accommodated by localized band structures in the rolled sample. The rolled material exhibits severe macroscopic plastic anisotropy with strictly two-dimensional shear patterns. When these bands approximately cover the gage section, the average Poisson's ratio on one surface approximates 1 and the

other surface shows no expansion with Poisson's ratio about 0. These values are consistent with the isochoric process of plasticity. In the extruded material that is supposed to exhibit transverse isotropy due to its texture, the Poisson's ratio on all surfaces is around the typical 0.5, i.e., both surfaces contract the same amount that is consistent with volume preservation.

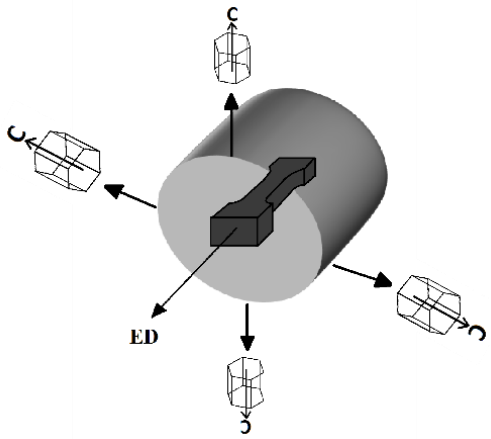

Figure 1.4. Extrusion Process – Preferred Orientation Of Hcp Crystals

1.2.3.1. Grain Size. Grain size has a strong influence on the mechanical properties of the materials. Yield strength of a polycrystalline material is inversely proportional to its grain size. The relationship is presented with Hall-Petch equation [7].

$$\sigma_y = \sigma_0 + k_y d^{-1/2} \tag{1.1}$$

where initial yield strength σ_0 and Hall-Petch slope k_y are material constants. The value of Hall-Petch slope depends on the deformation mechanism that causes yielding of the material. It is stated that k_{yT} (slope for twinning dominated deformation), has a higher value than k_{yS} (slope for slip dominated deformation) [8, 9]. This implies that the effect of grain size is more pronounced when yielding is governed by twinning.

Twins are mainly formed at gain boundaries which could be a nucleation place for both neighboring grains. The neighboring twins are called "cross-boundary twins" which could be nucleated at the same time or activated by the formation of the other. Their presence indicates "auto-catalytic" twin nucleation and observed in studies on twin transmission [10–

16]. According to the microscopic observations of Barnett *et al*. (2012) [12] and Ghaderi *et al*. (2011) [13], the number of cross-boundary twins increases as grain size decreases. Combined neutron diffraction and acoustic emission studies of Muránsky *et al*. (2010) [14, 15] also reports that collective twin nucleation is more prominent in fine grained ZM20 Mg alloy than the coarse grained one. Twin growth is the main strain accommodation mechanism and nucleation occurs gradually at the coarse-grained alloy with load increase. It is also stated that twin nucleation stress is greater for the finer grained samples. This means, inverse proportional relationship between grain size and yield strength can be attributed to higher twin nucleation at finer-grained materials [13].

The grain size of a polycrystalline naturally has a distribution about the nominal/average value. It is stated that twin nucleation does not depend on the grain size distribution in a sample – though it showed strong dependence on the nominal grain size. It is consistently claimed that grain size variation does not influence twin transmission [16, 27, 28].

1.2.4. Twin volume fraction

Twin volume fraction is a measure to determine the role/fraction of twinning in deformation. There are several ways to measure twin volume fraction experimentally. EBSD studies on Mg AZ31 alloy reports various area fractions of twinning: 35% in an extruded sample at nominal strain $\varepsilon_M = 4\%$ [29], 80% in a rolled sample ($d{\sim}13\mu m$) at $\varepsilon_M = 11\%$ [30], 20% in a rolled sample (d~30μm) at $\varepsilon_M = 1.5\%$ [31]. The results of neutron diffraction investigations on Mg AZ31 show that twin volume fractions are about 10% in an extruded sample at $\varepsilon_M = 1.4\%$ [32] and 72% in a rolled sample ($d{\sim}50\mu m$) at $\varepsilon_M = 5\%$ [1]. Ghaderi and Barnett used different grain sized ($d{\sim}5-55\mu m$) samples and found that the average twin volume fraction is about 25% at $\varepsilon_M = 1.5\%$ by using EBSD and optical microscopy [13]. Muransky *et al*. (2010) [14] states that the volume fraction is found about 20% at $\varepsilon_M = 1.5\%$ for both fine grained ($d = 17 \pm 10\mu m$) and coarse grained ($d = 114 \pm 49\ \mu m$) samples by using neutron diffraction and acoustic emission. Common findings of these studies: i) the value of twin volume fraction is not noticeably affected by

grain size but rather depends on the sharpness of texture. ii) twin volume fraction increases with macroscopic strain.

Contribution of twinning is formulized by relating total strain generated by twinning to characteristic twinning shear (γ_t) twin volume fraction (V_t) and an effective Schmid factor ($\bar{m}$) [10, 12, 13]

$$\varepsilon_t = \gamma_t \cdot \bar{m} \cdot V_t \tag{1.2}$$

1.3. Scope

The method precursor of this study is Aydıner and Telemez [21] which implements an area-scanning version of microscopic DIC to gather strain maps at crystallite resolution but with entire sample coverage. They analyzed rolled Magnesium AZ31 over the tensile twin plateau and this is another specific that is shared by the current work. This work builds upon Aydıner and Telemez [21] by investigating the grain size dependence of tensile-twin dominated Mg AZ31 deformation. For this purpose, two samples are cut from rolled plate: i) one as-received, fine-grained (FG) sample ii) one heat-treated, coarse-grained (CG) sample. The samples are tested under compressive loading that activates tensile twinning. Resultant deformation maps are used to compare strain heterogeneity of the samples at macroscopic and microscopic scales. Formation and expansion of the deformation structures are evaluated with detailed examination of the maps.

One other aspect of the study that is distinct from Aydıner and Telemez [21] is the quantitative focus on shear bands structures. Though the shear band structures stem from propagating twin activity, they are not monolithic twin transformation zones; namely, only a certain volume fraction inside the bands undergoes twinning. An important part of this study is to try to quantify the twinning activity inside the bands over strain results. Accordingly, the strain content of the deformation bands is examined apart from the undeformed regions by geometric filtering. Two statistical approaches are used to find contribution of twinning to deformation inside the bands: i) Calculating twin volume fraction based on the average strain accommodated by the bands; ii) filtering the strain data

over the bands by threshold strain values (data filtering in addition to geometric filtering). Data filtering will also be implemented over the entire gage section for sample scale quantitative results. All these analyses will be implemented over both FG and CG samples to investigate potential grain size effects.

2. EXPERIMENT

2.1. Sample Preparation

2.1.1. Material Properties

Bulk rolled material of Mg AZ31B was procured from Xi'an Yuechen Metal Products Co., Ltd., China in the form of rolled plate. Average grain size of the as-received material is found ~11μm by linear intercept method. Orientation distribution was identified with a Panalytical X-Pert Pro MPD four-cycle diffractometer. Pole figures were obtained by MTEX analysis (See Figure 2.1).

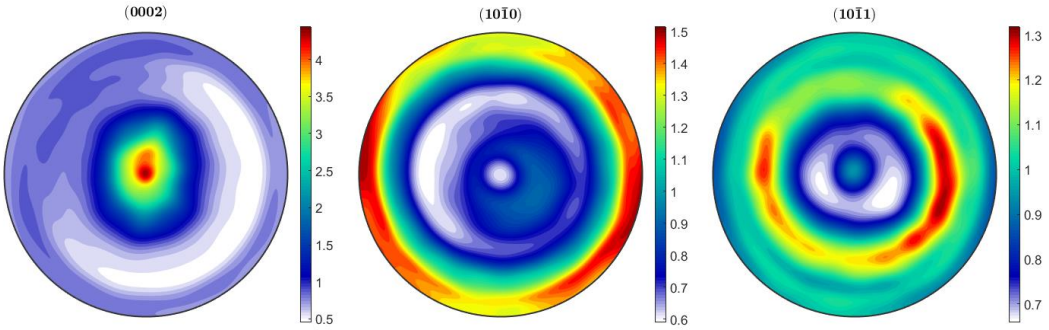

Figure 2.1. Pole Figure of Rolled Material

This study is parameterized over as received and enlarged grain size. The bulk material is heat treated at 500°C for 4 hours *in vacuo* to obtain enlarged grain. Heat treatment is done before machining of the sample to avoid surface oxidation and to obtain better uniformity of the resultant grain size. Resultant average grain size is 25 μm.

2.1.2. Sample Geometry

Two dog bone samples are cut from as-received (fine-grained - FG) and heat treated, (coarse grained - CG) material by electro discharge machining with the dimensions shown in Figure 2.2. Both samples are cut from the interior of the bulk material. Observation

surface of the sample is parallel to the $TD^{\perp}$ plane of the plate. Loading direction is aligned with RD (See Figure 2.3).

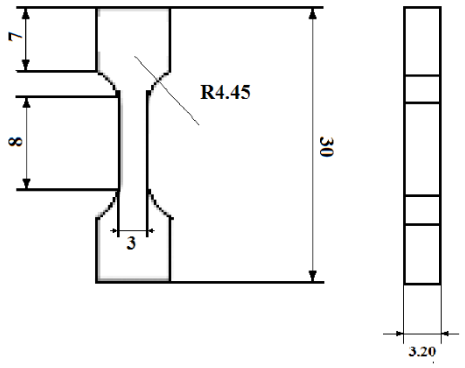

Figure 2.2. Sample dimensions

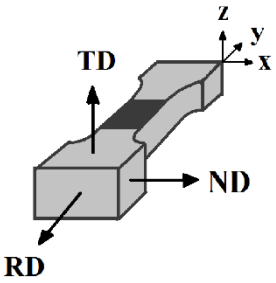

Figure 2.3. Observation surface is on RD plane (RD: rolling direction, ND: normal direction, TD: transverse direction)

2.1.3. Surface Preparation

2.1.3.1. Metallography. The samples are mounted in resin before grinding. Mounting the sample prevents from introducing and incline on the surface during grinding. It also helps avoid twin formation prior to experiment. Observation surface of the sample is ground with P800, P1000, P1200 and P2500 grade sandpapers. The samples are ground until the major flaws of the surface are eliminated. After grinding, the samples are mechanically polished to remove remaining scratches. The next step is etching the sample surface to expose the grain boundaries. The etchant solution contains 0.64gr picric acid, 15 mL ethanol, 1.5 mL

distilled water, and 1.5 mL acetic acid. The top surface of the sample is immersed in the solution for 2 seconds. To prevent any overexposure, the sample surface is rinsed with ethanol thoroughly.

2.1.3.2. Speckle pattern application. The top of the sample surface is painted with an Iwata airbrush using a solution of black paint and water. It is applied from a distance of 10 cm at 4 bars pressure. Figure 2.4 shows a region before and after the application of speckle pattern. The specifications required on the speckle pattern is explained in the Section 2.2.2 - DIC Application.

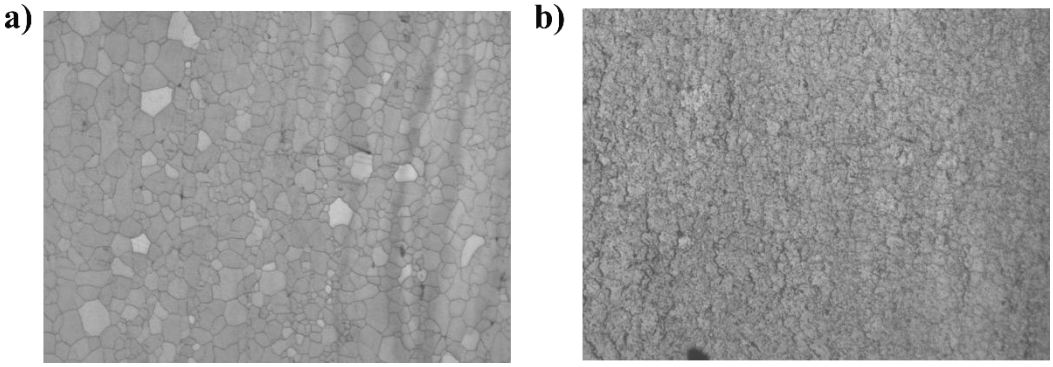

Figure 2.4. Speckle Pattern before (a) and after (b) painting

2.2. Experimental Setup

2.2.1. Setup

The elements of experimental setup are shown in Figure 2.5. The experiments are conducted on a Kammrath&Weiss microscopic tension-compression loading module. Newport-ILS positioning stages are used to set the height of the sample in an autofocusing implementation (Z-direction), and also locating module between two optical lines (X-Y plane), called macro-DIC and micro-DIC. Motions of the stages are controlled by an in-house computer code. Macro-DIC and micro-DIC optics utilizes the same type of camera, Allied Vision Pike-F505 CCD (2452x2054 pixels). Macro-DIC camera is coupled with an Edmund Optics 0.5x telecentric lens resulting in 6.8 μm/ pixel resolution. Micro-DIC optical

line is composed of a Navitar 60191D zoom lens (set at 4x) and a Mitutoyo 10x infinity corrected objective, amounting to an optical resolution of 0.19 μm/ pixel. Camera system is fixed on an Aluminum frame and the all imaging, positioning and loading elements of the setup sit on a Newport optical table to ensure vibration damping and isolation. The sample is placed in the loading module as in Figure 2.6(a) by tightening the grips (Figure 2.6 (d)).

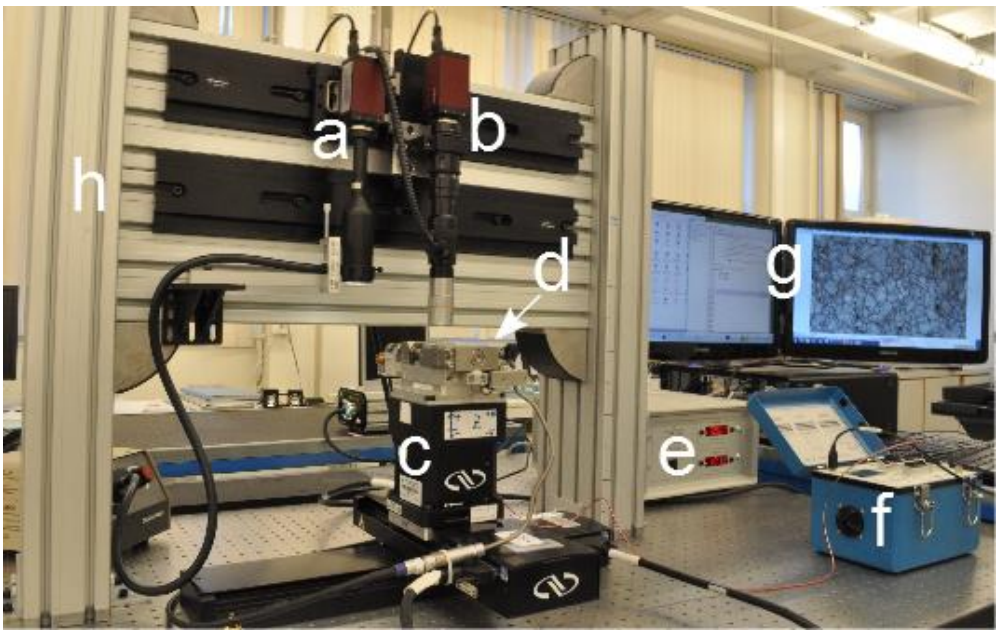

Figure 2.5. Experimental setup: (a) macro-DIC optics, (b) micro-DIC optics, (c) positioning stages, (d) micro tensile/compression loading module, (e) controller of the loading module, (f) strain gage data acquisition module, (g) computers, (h) Aluminum frame

2.2.2. DIC Application

Digital image correlation (DIC) is a deformation/displacement measurement technique that operates by comparing two images of a sample. The comparison is conducted between the images that belong to the first load point (reference) and a desired load point in the experiment. Therefore, the images in comparison are called undeformed and deformed images.

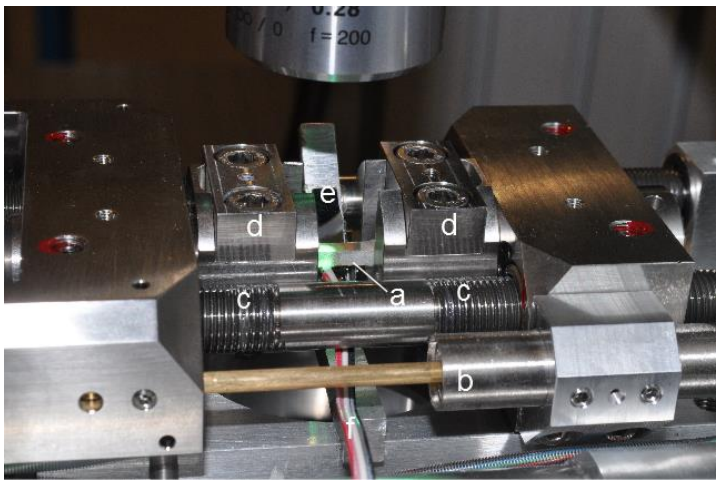

Figure 2.6. Elements of the setup about the loading stage (a) Sample, (b) LVDT transducer, (c) power screws, (d) grips, (e) mirror

Gray-scale images recorded in this study can be represented as intensity matrices (ex. 2452x2054 in this study) whose elements correspond to detector pixels. Each pixel has a gray value varying between 0 and 255. Finding the location of a single pixel from undeformed image in the deformed one is impossible, because there may be many pixels having the same grey value. Therefore, DIC analysis is performed by searching for a small neighborhood, a subset, of pixels with a characteristic pattern. Thus, the pattern has a critical role in the operation of DIC method. The quality of a pattern is measured by its signal content. For a patterned image, the grey values of the pixels must have a normal distribution with high dynamic range. To produce such a pattern, the sample surface is painted with an airbrush after etching. The spray of airbrush introduces a suitable particle size for DIC application over multiple length scales [17, 21, 33].

DIC analysis is conducted over an equally spaced grid on the sample surface defined over the undeformed image. Grid points are the centers of each DIC subset. DIC tracking of each subset on the deformed image provides displacement field (u, v) of grid points at position (x, y). The displacement field is differentiated to obtain strain and rotation by the central difference method to generate the corresponding deformation maps [21]:

$$\varepsilon_{xx} = \frac{\partial u}{\partial x} \tag{2.1}$$

$$\varepsilon_{yy} = \frac{\partial v}{\partial y} \tag{2.2}$$

$$\varepsilon_{xy} = \frac{1}{2}\left(\frac{\partial u}{\partial y} + \frac{\partial v}{\partial x}\right) \tag{2.3}$$

$$\omega_{xy} = \frac{1}{2}\left(\frac{\partial u}{\partial y} - \frac{\partial v}{\partial x}\right) \tag{2.4}$$

Further details on of DIC and its application can be found in [17]. Here, the subset size and the distance between two adjacent grid points are, 81 pixels (~551 μm x 551 μm) and 20 pixels for the macro-DIC analysis (see Figure 2.6a) and 61 x 61 pixels (~12 μm x 12 μm) and 10 pixels for micro-DIC analysis (see Figure 2.6b).

Recall the average grain size for FG and CG samples are 11 μm and 25 μm to compare with the measurement length scale. One deduces that the micro-DIC analysis provides a coarse sub-grain resolution for CG sample, while it has a grain scale resolution for the FG sample.

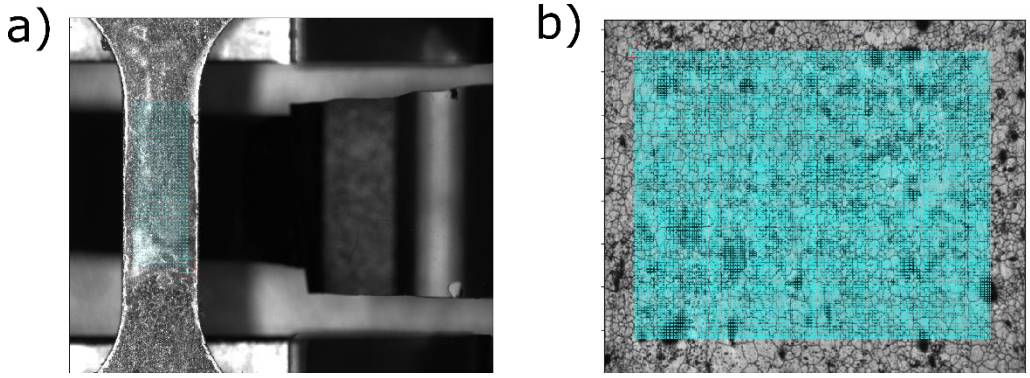

Figure 2.7. Grid structure of (a) a macro-DIC image, (b) micro-DIC image (~35000 points)

Full-field measurement at the sample scale in the microscopic resolution is achieved by area-scanning the sample under the objective for a $6x16$ matrix of overlapping images. The ~500 pixels overlap aims to obtain continuous strain maps. DIC analysis is performed individually for every image in a micro-DIC scan. To stitch the images and the strain maps successfully, the locations of individual frames are identified on a unique sample coordinate

system that sits on the upper left corner of the overall microscopic DIC coverage. This coordinate system is in mm, derived from the Newport X-Y stage positions recorded by the instrumentation software. Thus, ultimately, a contiguous strain matrix is generated for every micro-DIC load point by the post-processing software. The resultant strain matrix represents the whole gage section by approximately 2.6 million data points (microscopic resolution over a macroscopic region). Once the data is stitched, macroscopic regions of interest of any shape and size can be considered and analyzed statistically (a significant improvement of this study over Aydıner and Telemez [21] without being limited to a singular micro-DIC frame.

2.2.3. Test Procedure

The test methodology is comprised of the following steps:

- The dimensions of the samples are measured before the experiment.
- Controllers of loading module and stages are turned on.
- Light sources and cameras are turned on. Alignment of optics is checked.
- Sample is placed in the loading module and the gage section is centered in the middle of grips.
- The sample is aligned vertically with the help of macro-DIC and micro-DIC optics.
- Grip screws are gradually tightened, and any imposed strain is relieved by opening or closing the jaws of the frame. This is achieved by keeping the load cell output around zero.
- Initial positions of micro-DIC and macro-DIC optics are specified. (Imaging script will manage visiting both stations at desired loads.)
- Z-stage position is set by the focus distance for both cameras. It is an initial guess for the micro-DIC implementation. (During the micro-scan, auto-focus operation is repeated by computer code before each frame is recorded.)
- The range of micro-DIC gage section is determined. Initial exposure time is detected for both cameras targeting 127 gray-scale averages.
- All parameters are entered to a settings file in python™ format.

- Imaging script is executed and macro-DIC and micro-DIC images of undeformed state are obtained.

  In the remaining stages, load is incremented very carefully in position control. In every load steps, the following steps are conducted:

- Macro-DIC imaging and analysis are implemented at every load point. Nominal strain is measured by immediate DIC analysis on this data. Stress is recorded from the load cell and the ensuing stress-strain plot is appended.
- Time consuming micro-DIC scans are conducted at representative stages of the loading. For Magnesium AZ31, events that, e.g., prompt a micro-DIC scan are the emergence of a new deformation band emerge or a sudden increase in the macroscopic strain.

In the experiments of this thesis, compressive load is gradually increased until macroscopic strain becomes nominal -2%.

3. RESULTS

3.1. Overall Mechanical Behavior

FG and CG samples are compressed along the rolling direction (Figure 2.3) until the nominal strain, ε_M, equals to -2% and -2.1%, respectively. Nominal strain ε_M is calculated by averaging ε_{yy} values obtained from macroscopic DIC analysis over the gage section (see Figure 2.6 for the corresponding DIC grid).

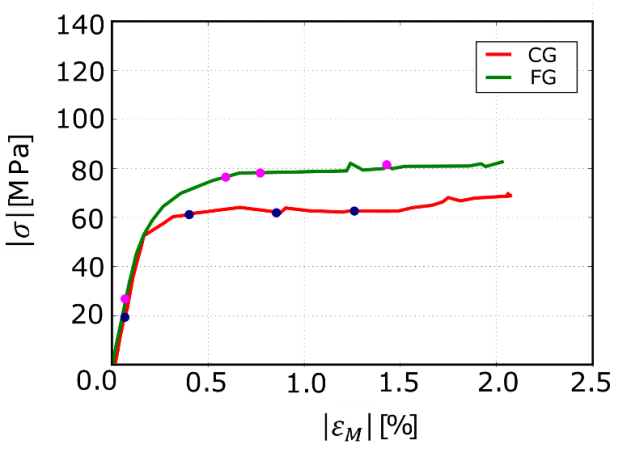

Figure 3.1. Stress-strain curves for both fine grained (FG) and coarse grained (CG) samples under uniaxial compression.

Absolute stress-strain (engineering stress, $|\sigma|$ vs. macroscopic DIC average, $|\varepsilon_M|$) curves of FG and CG samples are shown in Figure 3.1 for the uniaxial compression experiments. As the plastic deformation proceeds, both curves follow a region of constant stress commonly called “twinning plataeu”, where twinning is the dominant deformation mechanism [1, 12, 13, 34] (Ghaderi 2011. Barnett 2004. Brown 2005. Barnett 2012). Twin plateau stress is ~60MPa and ~80 MPa for CG and FG samples respectively.

FG sample exhibits a more abrupt transition to a near perfectly-plastic deformation whereas CG sample displays hardening at the onset of plasticity from 0.25%-0.6%. Since the deviation from linearity in each case approximately corresponds to the same stress,

samples do not show the Hall-Petch trend in terms of yield point. However, the grain size effect is manifested in the twin plateau stresses.

3.2. Analysis of Full-field Strain Maps

3.2.1. Strain Localization Patterns

Macroscopic DIC analysis results (Figure 3.2 and Figure 3.3) show that initiation and progression of plasticity are correlated with formation and expansion of localization patterns. The total strain is accommodated in ±45° inclined bands that emerges at $\varepsilon_M = 0.27\%$ and $\varepsilon_M = 0.3\%$ strains at FG and CG samples, respectively. This type of deformation heterogeneity has been observed and explained by Aydıner and Telemez (2014) [21] and Kapan *et al*. (2010) [20] as the indication of "locally-coordinated" simple shear processes associated with tensile twinning on rolled samples. Although heterogeneous deformation is observed on both FG and CG samples, macroscopic DIC results indicate that deformation bands have certain differences in nature.

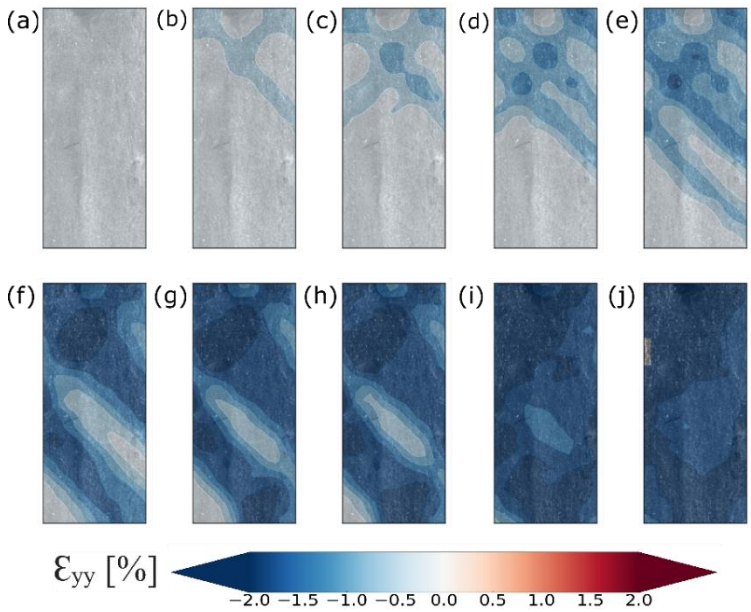

Figure 3.2. Macro DIC strain maps of FG sample at $\varepsilon_M =$ (a) -0.16%, (b) -0.27%, (c) -0.39%, (d) -0.6%, (e) -0.78%, (f) -1.42% (g) -1.61% (h) -1.69% (i) -2.01% (j) -2.16%

Starting from the emergence of localization patterns, distinct properties of deformation bands are observed among the FG and CG samples. At this stage, FG sample (Figure 3.2b, c) has a more dispersed deformation pattern comprising ±45° inclined cross-bands whereas the bands are unidirectional and more localized in the CG sample (Figure 3.3b, c). As the plasticity proceeds, FG sample accommodates the total strain by formation of new deformation bands (Figure 3.2d, e) while CG sample responds through the expansion of existent bands (Figure 3.3d, e). As the strain increases further, bands expand, merge and ultimately cover the gauge section in both samples (Figure 3.2f-j and Figure 3.3f-j).

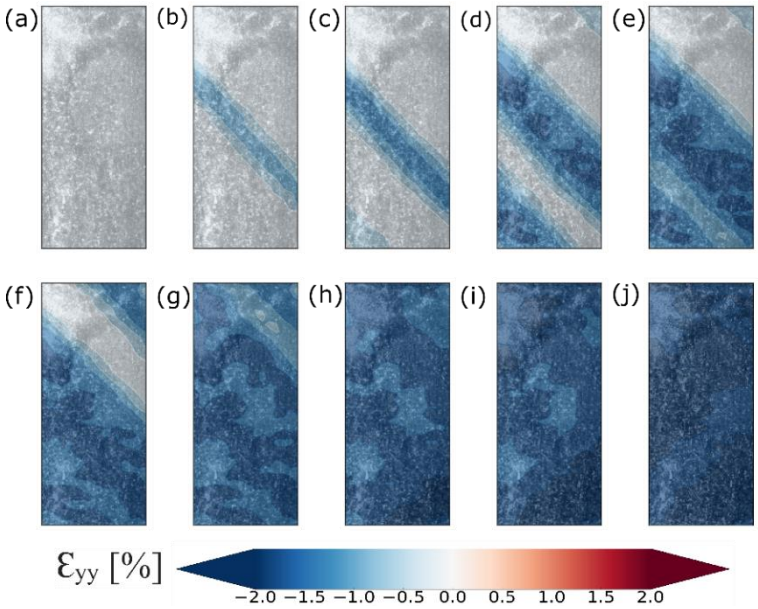

Figure 3.3. Macro DIC strain maps of CG sample at ε_M = (a) -0.14%, (b) -0.3%, (c) -0.43%, (d) -0.85%, (e) -1.06%, (f) -1.24% (g) -1.55% (h) -1.71% (i) -1.84% (j) -2.08%

Macroscopic strain maps in Figure 3.2b, c, d, f, j and Figure 3.3a, d, e, f, j are paired with the microscopic results of the same load points and provided in Figure 3.4 and 3.5. This demonstrates the effect of DIC length scale in displaying the details inside the deformed regions. Micro-scale strain maps show that, inside the deformation bands of the CG sample, strain is distributed homogeneously while localizations are more pronounced in FG sample. Especially in cross-band regions of FG sample, deformation is visibly more concentrated than the rest of the band. Another main difference can be observed at the final load points in Figure 3.4e and Figure 3.5e. Even when the nominal strain $\varepsilon_M \cong 2\%$, FG

sample has still dormant (undeformed) regions whereas the gauge section of CG sample is covered.

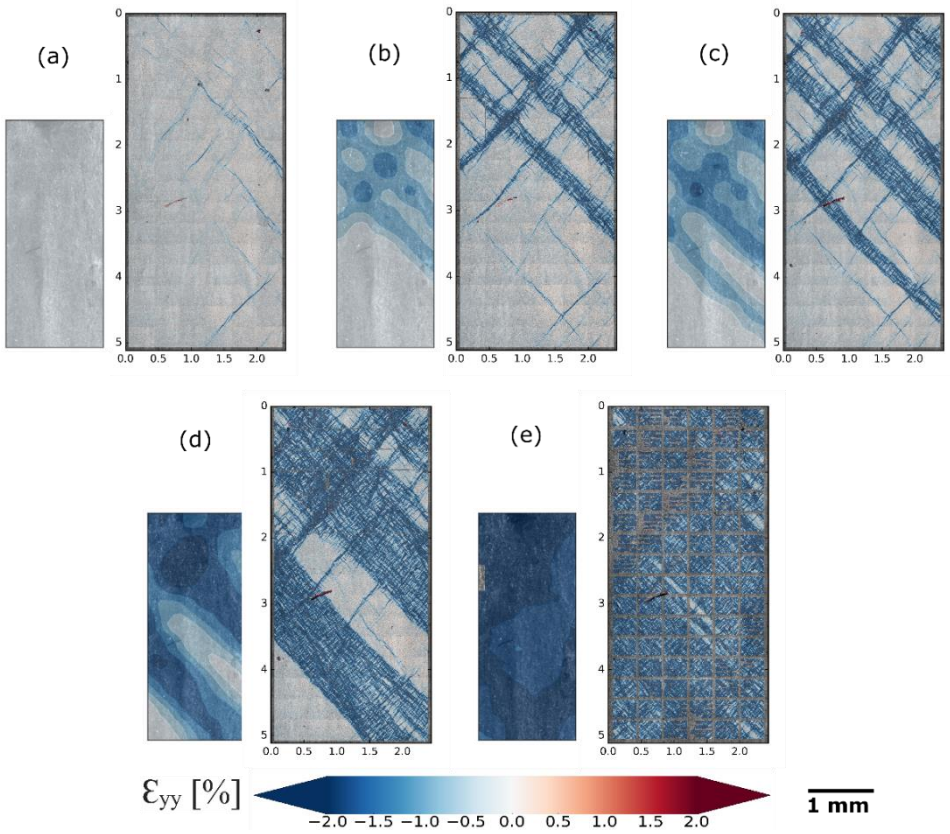

Figure 3.4. Macro and micro DIC strain maps of FG sample at ε_M = (a) -0.16%, (b) -0.6%, (c) -0.78%, (d) -1.42%, (e) -2.16%

3.2.2. Statistical Analysis of Localization Bands

To identify the grain size effects in detail, localization bands are analyzed quantitatively. The aim is to isolate the strain data of deformed regions from the rest of a map. Having a contiguous strain matrix at sample coordinates (Section 2.2.2) allows a numerical implementation to mask the desired region on the sample surface and extracting the data of only this region. Masked deformation bands and corresponding ε_{yy} histograms are provided in Figure 3.6-9, labeled with the same "band" numbers. $\bar{\varepsilon}_{yy}$ and $\bar{\varepsilon}_{xx}$ are obtained by averaging micro-DIC strains ε_{yy} and ε_{xx} inside the masked regions and, thus, are the average band strains provided in Table 3.1-2. To demonstrate the vast difference in

the strain content of deformed regions and the rest, a dormant area is also masked. Average strain in this region equals to -0.12% while it reaches to -1.74% in the bands at the same load point. Figure 3.6a-3 also shows the strain distribution of this area is around zero.

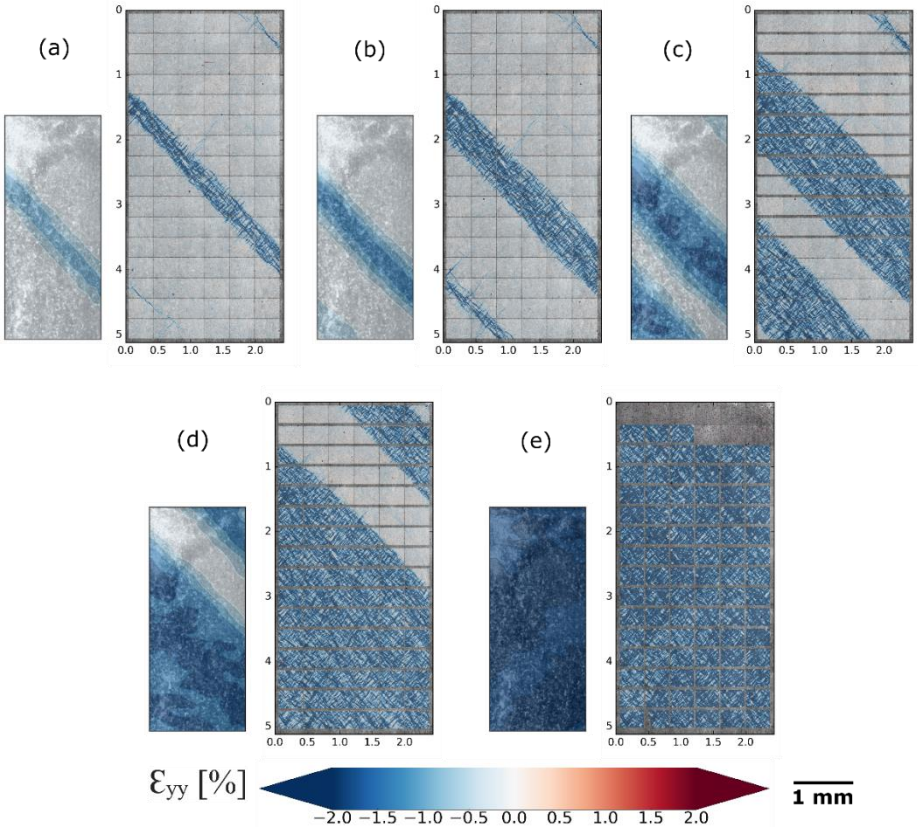

Figure 3.5. Macro and micro DIC strain maps of CG sample at ε_M = (a) -0.3%, (b) -0.43%, (c) -0.85%, (d) -1.24%, (e) -2.08%

In the FG sample, the additional strain between $\varepsilon_M = -0.6\%$ and -0.78% is accommodated by the newly formed deformation band (Figure3.6a-b). The widths of the previously-formed bands show limited expansion while their total strain average remains virtually constant (-1.73% vs -1.74%, see Table 3.1).

In the CG sample, as the existent bands expand as the strain increases from $\varepsilon_M = -0.6\%$ to -0.78% (Figure 3.7a-b), the average strain of deformed regions again increases imperceptibly from -1.54% to -1.58% pointing to a characteristic value.

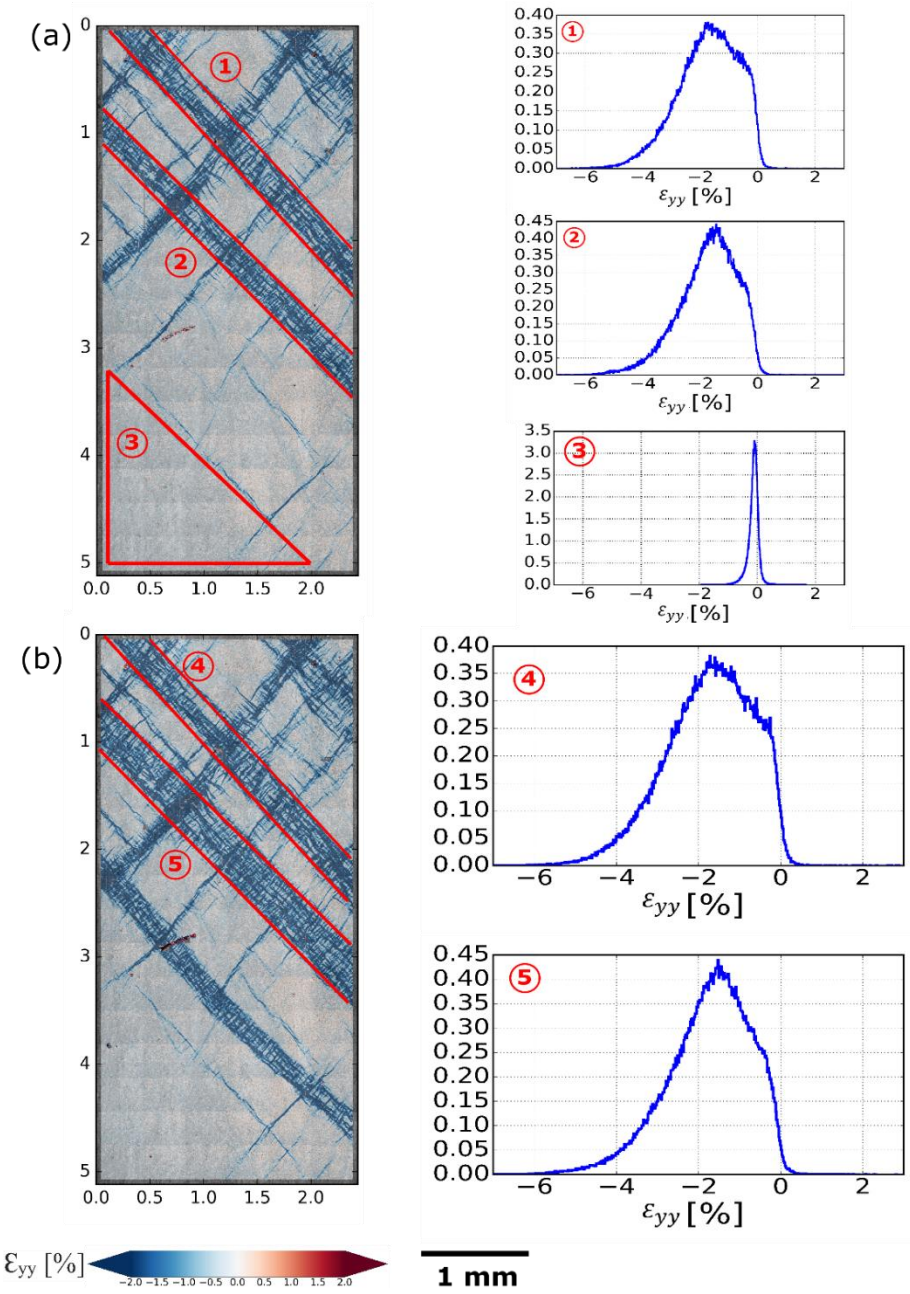

Figure 3.6. Masked deformation bands and the histograms of masked regions of FG sample at ε_M = (a) -0.6%, (b) -0.78%

In both samples, ε_{yy} histograms of newly formed deformation bands are wide and scattered reaching absolute maximum values of about 6%, incidentally close to the twin transformation strain 6.5%. This indicates intense microstructural strain heterogeneity inside the deformation bands (Figure 3.6a-1-2, Figure 3.7a-1, b-3, Figure 3.9a-1). The strain

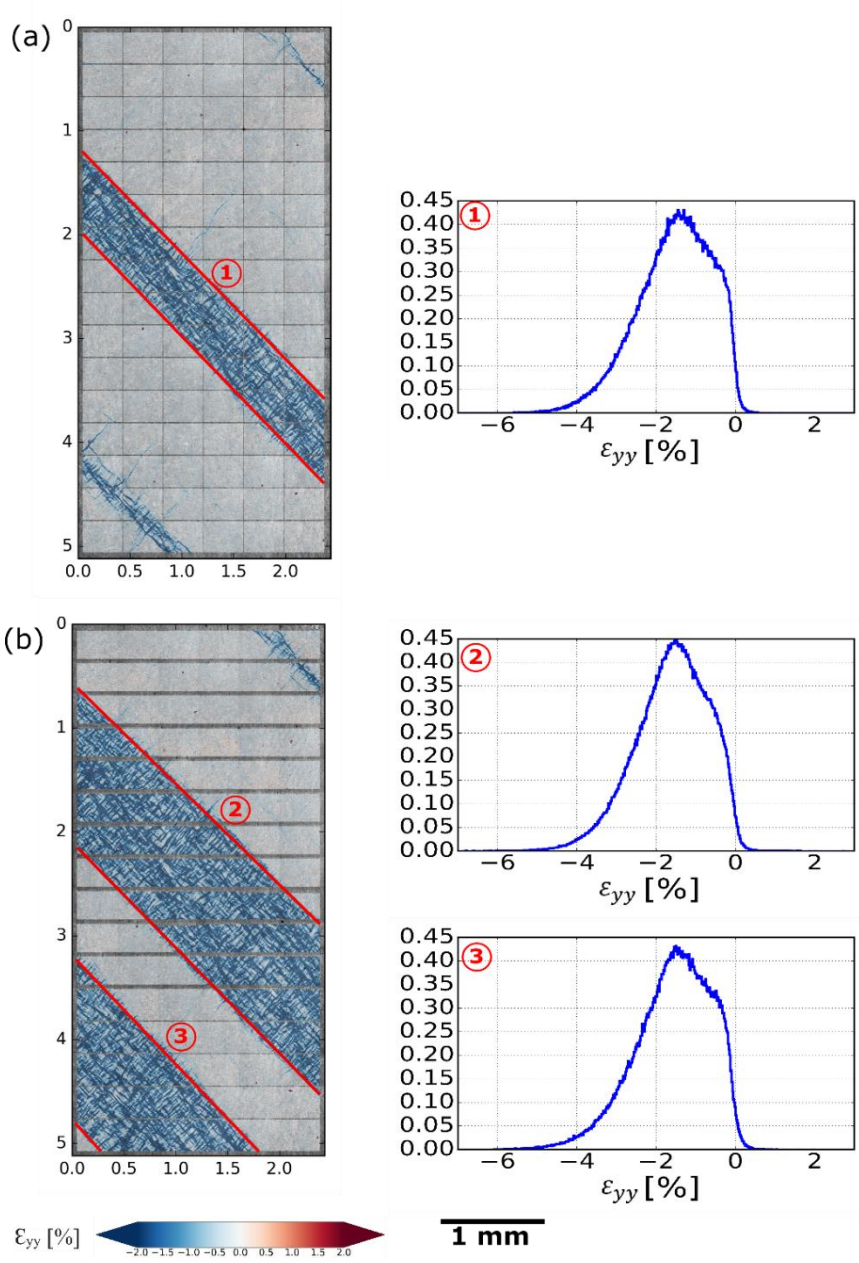

Figure 3.7. Masked deformation bands and the histograms of masked regions of CG sample at ε_M = (a) -0.43%, (b) -0.85%

distribution is lopsided with remnants of a zero-strain peak that belongs to locally dormant points. As the strain increases, deformation bands expand, and merge and the distribution get closer to a symmetric normal distribution in both samples (Figure 3.7-2, Figure 3.8a-1-2). The expansion and merging start earlier in the CG sample while the inside-the-band heterogeneity is preserved in FG at earlier steps (Figure3.6b4-5).

Until the point that deformation bands cover the gauge section, average band strains follow a stable trend around -1.55% in CG sample while the values increase and $\bar{\varepsilon}_{yy}$ reaches -1.9% at $\varepsilon_M = -1.42\%$ with macroscopic strain in FG sample. $\bar{\varepsilon}_{yy}$is always larger in FG sample compared to CG sample throughout the experiments. When deformation covers the gage section $\bar{\varepsilon}_{yy}$become nearly equal to the macroscopic strain $\bar{\varepsilon}_{yy}$in both samples.

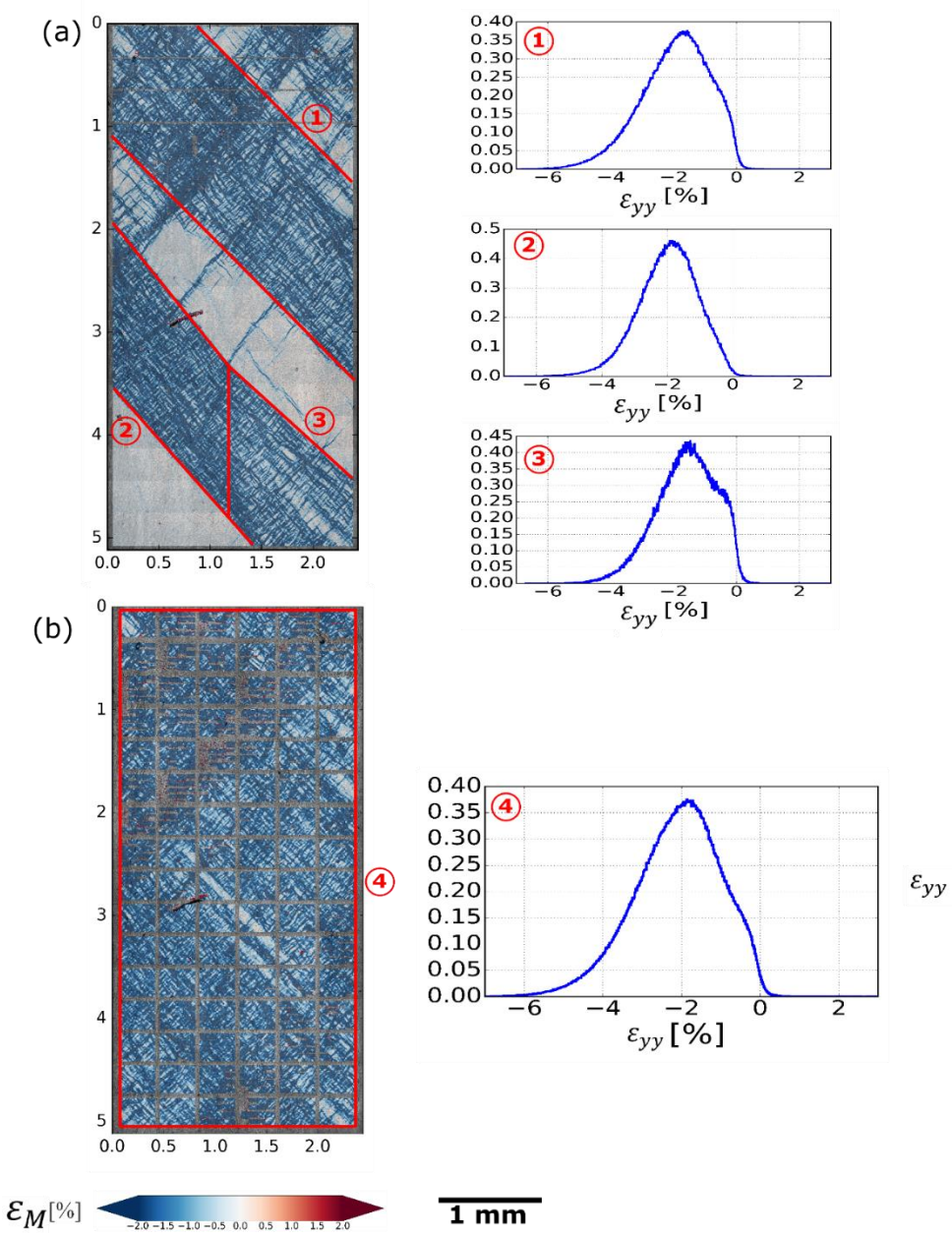

Figure 3.8. Masked deformation bands and the histograms of masked regions of FG sample at $\varepsilon_M =$ (a) -1.42%, (b) -2.16%

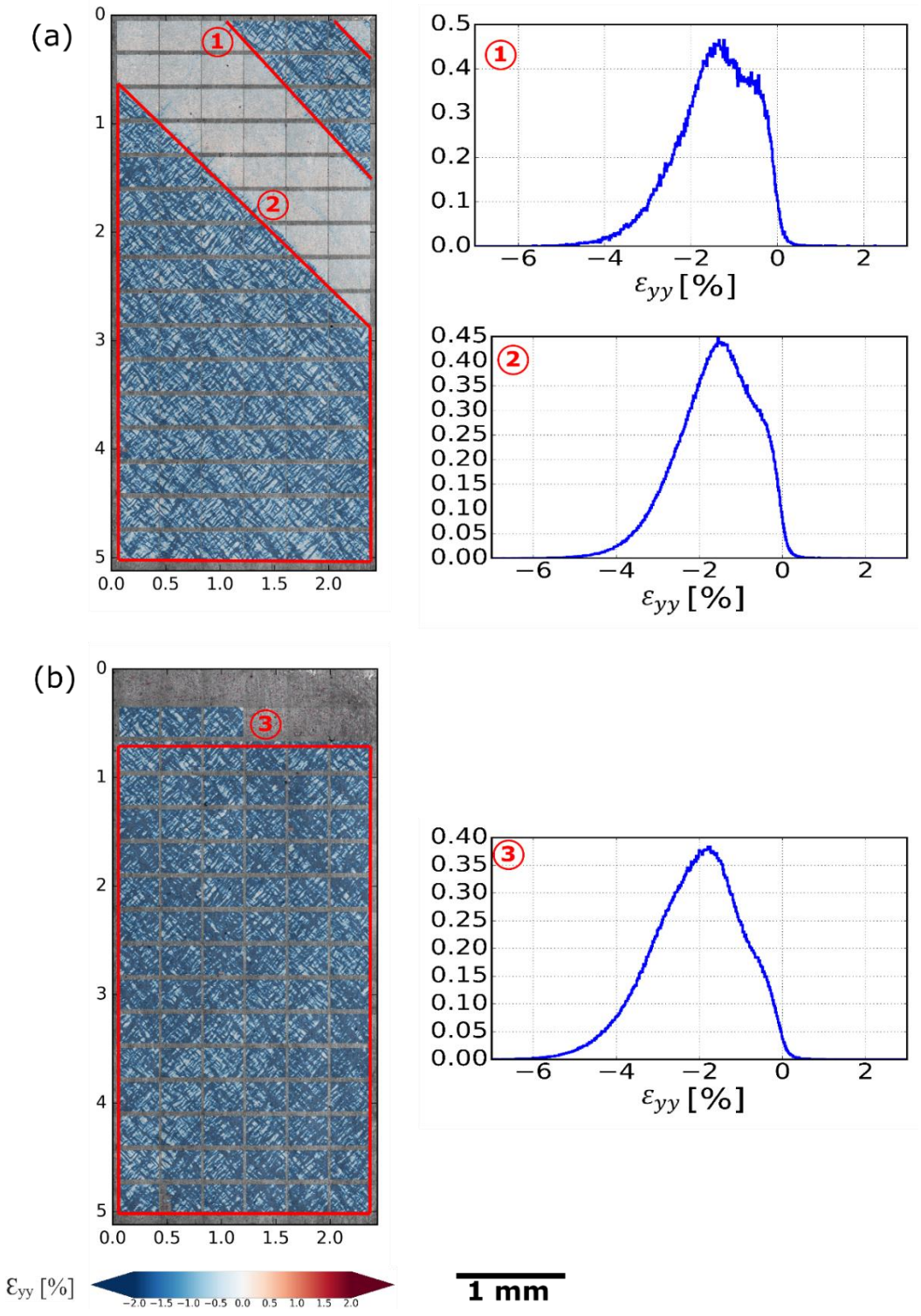

Figure 3.9. Masked deformation bands and the histograms of masked regions of CG sample at ε_M = (a) -1.24%, (b) -2.08%

Table 3-1. Average micro-DIC normal strains in y-direction, $\bar{\varepsilon}_{yy}$ (%), in x-direction, $\bar{\varepsilon}_{xx}$ (%); standard deviation of the axial micro-DIC strain distribution, ε_{yy}^{std}, and Poisson's ratio,ν_{xy}, defined over individual masked bands of FG sample (bands in Fig. 3.6 and Fig. 3.8) at various stages of loading specified by sample strain, ε_M.

Sample	$\boldsymbol{\varepsilon_M}$ **(%)**	**Band #**	$\bar{\boldsymbol{\varepsilon}}_{\boldsymbol{yy}}$ **(%)**	$\boldsymbol{\varepsilon_{yy}^{std}}$	$\bar{\boldsymbol{\varepsilon}}_{\boldsymbol{xx}}$ **(%)**	$\boldsymbol{\nu_{yx}}$
FG	-0.14	No band	-	-	-	-
	-0.60	1	-1.7300	1.0551	1.6979	0.9814
		2	-1.7367	1.0121	1.6899	0.9731
		3*	-0.1276	0.1810	0.07456	0.05109
	-0.78	4	-1.7496	1.0612	1.6936	0.9680
		5	-1.7473	1.0244	1.7181	0.9833
	-1.42	1	-1.9521	1.1005	1.9286	0.9879
		2	-1.8268	0.9557	1.7811	0.9750
	-2.16	All surface (4)	-2.1071	1.1293	2.0870	0.9905

*Average strain of a dormant area

Table 3.2. Average micro-DIC normal strains in y-direction, $\bar{\varepsilon}_{yy}$ (%), in x-direction, $\bar{\varepsilon}_{xx}$ (%); standard deviation of the axial micro-DIC strain distribution, ε_{yy}^{std}, and Poisson's ratio,ν_{xy}, defined over individual masked bands of CG sample (bands in Fig. 3.7 and Fig. 3.9 at various stages of loading specified by sample strain, ε_M.

Sample	$\boldsymbol{\varepsilon_M}$ **(%)**	**Band #**	$\bar{\boldsymbol{\varepsilon}}_{\boldsymbol{yy}}$ **(%)**	$\boldsymbol{\varepsilon_{yy}^{std}}$	$\bar{\boldsymbol{\varepsilon}}_{\boldsymbol{xx}}$ **(%)**	$\boldsymbol{\nu_{yx}}$
CG	-0.16	No band	-	-	-	-
	-0.43	1	-1.5402	0.9395	1.4624	0.9495
	-0.85	2	-1.6031	0.9144	1.5452	0.9639
		3	-1.5693	0.9248	1.5211	0.9692
	-1.24	1	-1.4505	0.8941	1.4156	0.9759
		2	-1.6134	0.9253	1.5653	0.9702
	-2.08	All surface (3)	-2.0846	1.0802	2.0667	0.9914

Despite the existence of the dormant regions inside deformation bands of FG sample, higher band average strains, $\bar{\varepsilon}_{yy}$, reveal an elevated level of heterogeneity with respect to the CG sample. Figure 3.6-7 shows that cross regions display more intense deformation in FG sample, which is expected as in these regions strain contents add up and rotations annihilate [20]. To quantify this, intersection regions are specifically evaluated as shown in Figure 3.10-12 and the corresponding average strains are provided in Table 3.3.

The total area of cross-regions increases with the strain. The average strains of these regions are always higher than the overall band averages (up to 1.3-1.7 times). The cross regions at ε_M = -0.6% (Figure 3.10a-b) are located at ε_M = -1.42%, (Figure 3.12b-c). The averages of the regions are calculated in the latter (within the former area coverage). These regions display still higher $\bar{\varepsilon}_{yy}$ than the rest of the intersection.

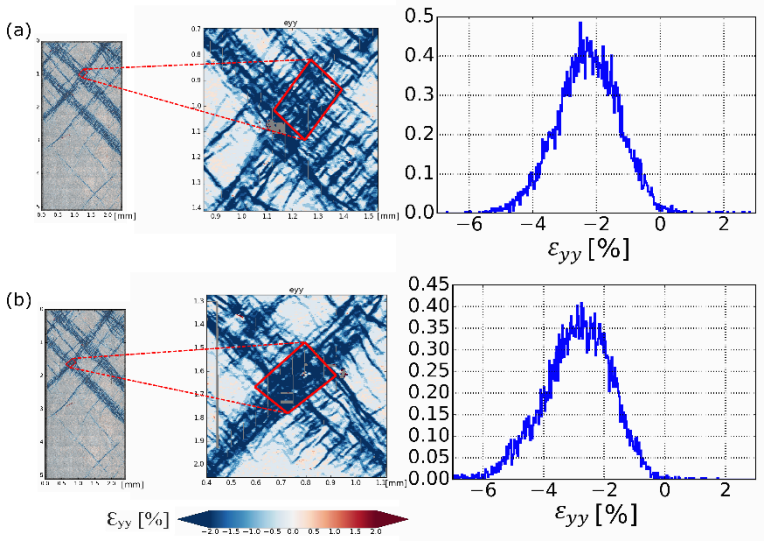

Figure 3.10. Masked cross regions and histograms for FG sample at ε_M = -0.6%

From ε_M = -0.6% to -0.78% cross region averages seem to remain roughly constant and even decrease to a limited extent against the expectations (Figure 3.10a-b and Figure 3.11a-b). One might speculate that cross regions undergo higher hardening than the rest of the sample and new strain accommodation is pushed away from these spots.

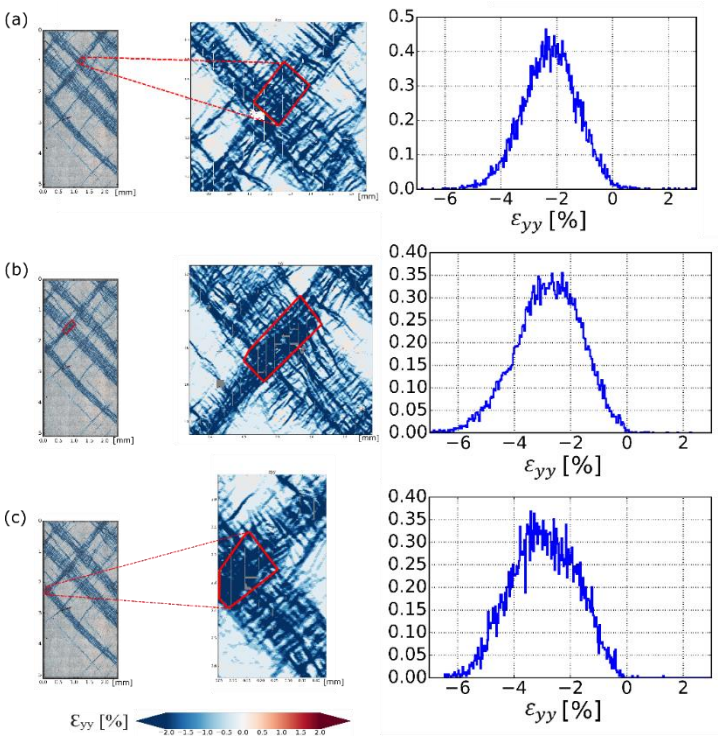

Figure 3.11. Masked cross regions and histograms for FG sample at ε_M = -0.78%

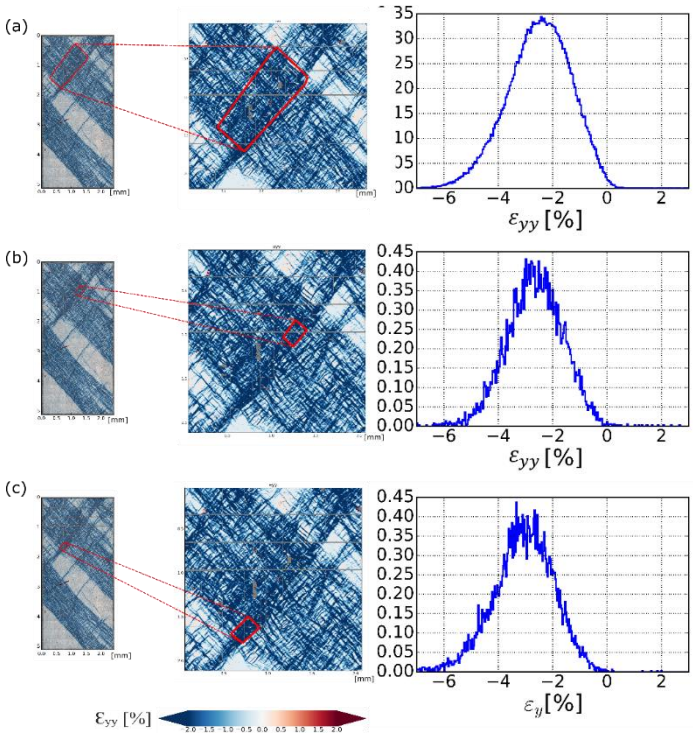

Figure 3.12. Masked cross regions and histograms for FG sample at ε_M = -1.42%

Table 3.3. Average micro-DIC normal strains in y-direction, $\bar{\varepsilon}_{yy}$ (%), in x-direction, $\bar{\varepsilon}_{xx}$ (%); standard deviation of the axial micro-DIC strain distribution, ε_{yy}^{std}, and Poisson's ratio,ν_{xy}, defined over band intersections in the FG sample (Figs. 3.10-12, a-c) at various stages of loading specified by sample strain, ε_M.

Sample	$\boldsymbol{\varepsilon_M}$ **(%)**	**Region**	$\bar{\boldsymbol{\varepsilon}}_{\boldsymbol{yy}}$ **(%)**	$\boldsymbol{\varepsilon_{yy}^{std}}$	$\bar{\boldsymbol{\varepsilon}}_{\boldsymbol{xx}}$ **(%)**	$\boldsymbol{\nu_{yx}}$
FG	-0.60	(a)	-2.2816	0.9885	2.3560	1.0326
		(b)	-2.9006	1.1276	2.7985	0.9648
	-0.78	(a)	-2.2548	0.9925	2.3234	1.0304
		(b)	-2.8034	1.1777	2.7424	0.9782
		(c)	-2.9395	1.1482	2.8634	0.9741
	-1.42	(a)	-2.5047	1.1687	2.5324	1.0110
		(b)	-2.6584	1.0521	2.7141	1.0209
		(c)	-3.0784	1.1246	2.9493	0.9580

3.2.3. In-plane Poisson's ratio over shear band structures

The last columns of Table 3.1-3 contain Poisson's ratios (ν_{yx}) for the selected deformed regions. ν_{yx} is obtained by using average strains $\bar{\varepsilon}_{yy}$ and $\bar{\varepsilon}_{xx}$. For isotropic plasticity, as well known, ν_{yx} would take the value of 0.5 same as ν_{yz} or contraction ratio on any other plane due to the isochoric (volume-preserving) nature of plastic deformation. On the other extreme, when an individual simple shear structure is observed and the observation plane x-y matches the plane of shear, ν_{yx} becomes 1 [20, 21]. The lack of contraction at the plane perpendicular to the observation surface can easily be proven:

$$\nu_{yx} = -\bar{\varepsilon}_{yy}/\bar{\varepsilon}_{xx} \cong 1 \;\Rightarrow \bar{\varepsilon}_{yy} + \bar{\varepsilon}_{xx} = 0 \tag{3.1}$$

$$\varepsilon_{xx} + \varepsilon_{yy} + \varepsilon_{zz} = 0 \;\Rightarrow \varepsilon_{zz} = 0\,;\; \nu_{yz} = 0 \tag{3.2}$$

The table clearly sites the ν_{yx} evaluated over the band structures takes a value of 1 with a nominal 3% error. (The values slightly above 1 is interpreted as experimental error.)

Since plastic deformation requires zero volumetric change, ε_{zz} becomes zero. Zero strain in z-direction (through the sample surface) means deformation occurs in xy-plane. Both FG and CG samples exhibit 2D deformation as a result of twinning dominant and anisotropic deformation specific to the rolling texture. Since this study is already focused on the deformed regions ν_{yx} is always around 1 supporting the study of Kapan *et al.* [20].

4. DISCUSSION

Strain maps of FG and CG samples indicate a grain size effect on the degree of heterogeneity at macroscopic and mesoscopic scales. The most prominent distinction is that CG sample deforms with disconnected singular strain localization structures whereas localization patterns form simultaneously with a cross network in the FG sample. Increasing load results in expansion and merging of deformed regions in both samples. CG sample accommodates strain by continuing enlargement of few detached bands. In the FG sample, borders of deformed regions are less well-defined than those in the CG sample, there are always cross connections between bands.

One may speculate that the macroscopic and mesoscopic localization patterns imitate the microscopic twinning nucleation and growth behavior with emergence and subsequent cascaded expansion. Collaborative twin nucleation (described as autocatalytic twinning in Section 1.2.3.2) is positively correlated with fine grain sizes according to Ghaderi *et al* (2011) [13] and Muransky *et al* (2010) [14]. Dispersed and cross-connected deformation patterns in FG sample may be an indication of typical collaborative twin nucleation seen in fine grained materials. Gradual expansion of the CG sample bands may suggest more progressive twin nucleation observed in coarse grained materials. Thus, distribution of deformation patterns might be related to grain size dependent microscale deformation mechanisms.

Both samples are compressed in the loading direction that favors twinning. Sudden emergence of localization patterns throughout the twin plataeu also confirms that dominant deformation mechanism is twinning. If it is assumed that twinning activity is the only deformation source, average strains ($\bar{\varepsilon}_{yy}$) can be utilized to determine an approximate twin volume volume fraction.

$$\bar{\varepsilon}_{yy} = \gamma_t \cdot m \cdot V_{STA} \tag{4.1}$$

where V_{STA} is defined here as sole-twin-activity volume fraction and $\gamma_t = 13\%$ is characteristic twinning shear posed by $\{10\bar{1}2\}\langle\bar{1}011\rangle$ tensile twin. It must be emphasized that V_{STA} is not the actual volume fraction of twins V_t as defined in Section 1.2.4 but an approximate value that bases all strain accommodation on twinning. The value of typical average Schmid factor, $\bar{m}$, is in the range of (0.4 - 0.5) for this texture/load combination [1, 35]. Strain averages ($\bar{\varepsilon}_{yy}$) are already known for selected deformation bands. Then,

$$V_{STA} = \frac{\bar{\varepsilon}_{yy}}{\gamma_t \cdot \bar{m}} \tag{4.2}$$

$$0.15\ \bar{\varepsilon}_{yy} \leq\ V_{STA} \leq 0.19\ \bar{\varepsilon}_{yy} \tag{4.3}$$

As the texture gets sharper Schmid factor m approaches to 0.5 that approximately corresponds to c-axes normal to the load direction for all grains. If equations 1.1 and 4.2 are combined, one finds

$$\frac{\varepsilon_t}{\bar{\varepsilon}_{yy}} = \frac{V_t}{V_{STA}} \tag{4.4}$$

If a single crystal material is loaded in the direction that favors twinning, the only source of deformation in a band is expected to be twinning, implying $V_{STA} = V_t$. In all other cases including this one, twin strain will be only a part of total strain, i.e., $\varepsilon_t < \bar{\varepsilon}_{yy}$. This implies that V_{STA} overestimates the actual twin volume fraction. Here, though, the averages are precisely taken over the bands that abruptly form with twin propagation. So, one might speculate that the values might be close. Here, V_{STA} is only used for the purpose of grain size comparison.

Average strains are calculated for every load point for the deformed regions and $m = 0.5$ is used for the Schmid factor. Until $\varepsilon_M = -2\%$, FG sample has a higher V_{STA} than CG al every load point but the values are comparable. Figure 3.13 indicates that, V_{STA} increases with macroscopic strain ε_M supporting the results of Ghaderi *et al*. (2011) [13].

V_{STA} remains constant on a singular band even when it expands, confirming the conjecture that band strain and corresponding V_{STA} are characteristic values. Only when bands intersect and interact, the strain in these localization structures rise noticeably.

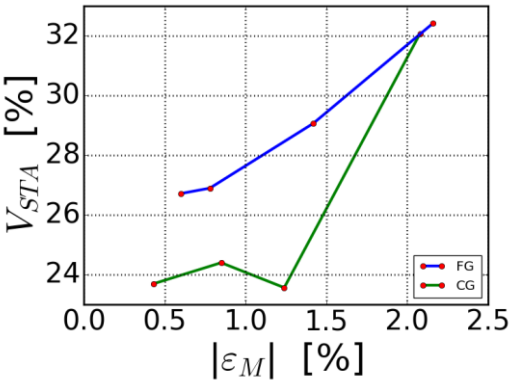

Figure 4.1 Sole-twin-activity volume fraction, V_{STA}, vs. absolute macroscopic strain, $|\varepsilon_M|$ for both fine-grained (FG) and coarse-grained (CG) samples.

4.1. Filtering Strain Data

Figure 4.1, with caveats on V_{STA} detailed before, suggest a twinning volume fraction between 24-30 % inside the shear bands. Then, with the assumption that there is limited slip plasticity at this point, it is suggested that 70-76% of the band material is dormant. This raises the question of possibly distinguishing the two populations inside the bands by further filtering in terms of strain data. It is plausible to expect high strains about twinned localities and small strains about the dormant points, although of course the innate DIC subset averaging (subset size ~12 μm) will smear the fields.

The following mask figure exemplifies the filtering that if one further picks $|\varepsilon_{yy}| > 3\%$ **inside a band** (initial band of CG sample selected here at $|\varepsilon_M| = 0.43\%$). In-house software marks the boundary of the picked $|\varepsilon_{yy}| > 3\%$ localities with yellow. Indeed, one sees that local strain band structures are highlighted inside yellow dotted lines in Fig 4.2a (see the blow-up, Fig 4.2b). It is hard, however, to assess that this filter is appropriate for identification of regions of significant twin activity. The 3% threshold feels arbitrary, and

the shown histogram of picked points (Fig. 4.2c) clearly shows that the cutoff does not coincide with any natural threshold and just slices the data populations. Unfortunately, the overall histograms do not present a clear point of separation that can be defined as the threshold strain that distinguishes locally dormant and deformed (twinned) regions.

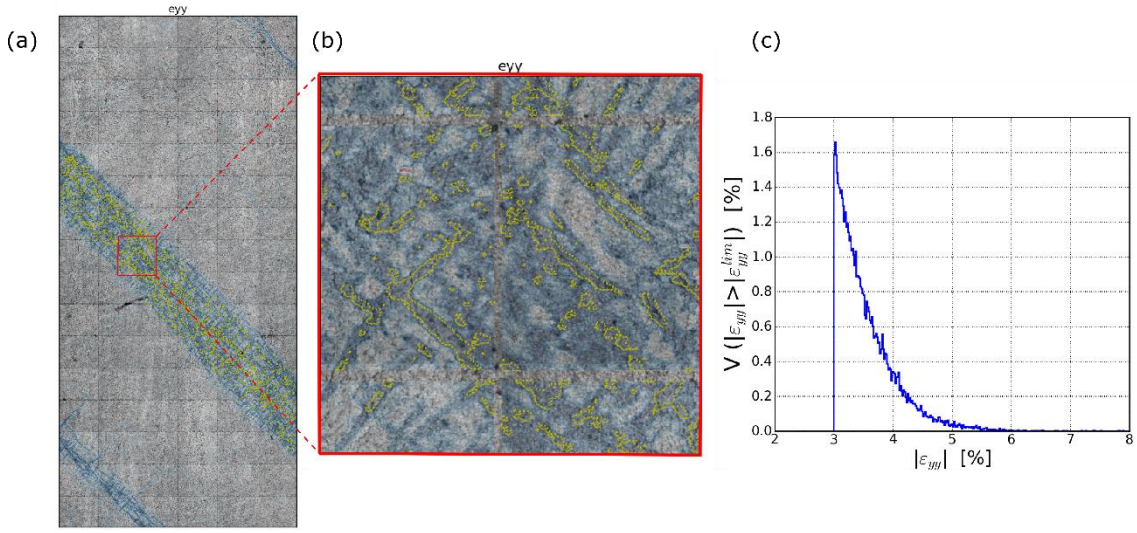

Figure 4.2 (a) Masked and filtered ($\left|\varepsilon_{yy}^{lim}\right| > 3\%$) deformation band of CG sample at $|\varepsilon_M| = 0.43\%$; (b) blow-up of filtered domains shown inside yellow boundaries ;(c) histogram of the filtered strain data

A comprehensive approach at this point is to parametrically assess threshold values, $\left|\varepsilon_{yy}^{lim}\right|$. For this the fraction (V) of the strain data filtered by the condition $\left|\varepsilon_{yy}\right| > \left|\varepsilon_{yy}^{lim}\right|$ is calculated for a continuous range of $\left|\varepsilon_{yy}^{lim}\right|$. Then $V\left(\left|\varepsilon_{yy}\right| > \left|\varepsilon_{yy}^{lim}\right|\right)$ vs. $\left|\varepsilon_{yy}^{lim}\right|$ is plotted to present the reader all possible threshold values. The resulting plots are akin to cumulative distribution functions (CDF) of probability distributions. Figure 4.3 shows this plot (blue curve) for the data points that fall inside the band presented in Fig. 4.2. This is essentially the CDF of the probability distribution function (PDF is the area normalized strain histogram) provided for this band (number 1 band) in Fig. 3.7. For the band results (blue curve), the V_{STA} value of approximately 24% brought over to estimate a twin threshold strain of $\left|\varepsilon_{yy}^{lim}\right| \approx 2\%$ over Fig. 4.3.

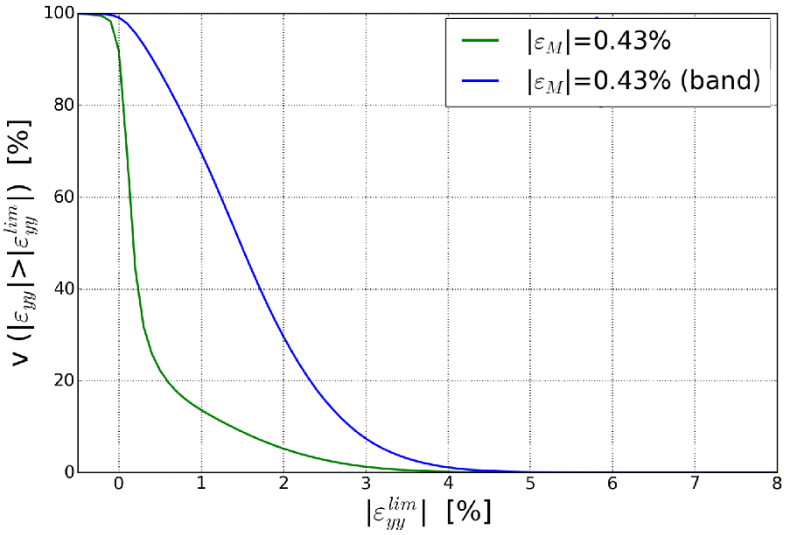

Figure 4.3 Fraction (V) of the number of filtered strain data points, ($|\varepsilon_{yy}| > |\varepsilon_{yy}^{lim}|$), to the number of the entire strain data plotted against $|\varepsilon_{yy}^{lim}|$ for CG sample within the masked band (blue curve) and all sample surface (green curve) at $|\varepsilon_M| = 0.43\%$.

As load is progressed with increasing $|\varepsilon_M|$, bands will cover more to gage section (practically the entire gage section by $|\varepsilon_M| \approx 2\%$) and CDFs will shift right. Figure 4.4 presents this transition over entire gage section $V(|\varepsilon_{yy}| > |\varepsilon_{yy}^{lim}|)$ vs. $|\varepsilon_{yy}^{lim}|$ plots for both CG and FG samples. The character of these CDFs are similar over both samples. As load is progressed with increasing $|\varepsilon_M|$, bands will cover more to gage section (practically the entire gage section by $|\varepsilon_M| \approx 2\%$) and cdfs will shift right. Figure 4.4 presents this transition over entire gage section with $V(|\varepsilon_{yy}| > |\varepsilon_{yy}^{lim}|)$ vs. $|\varepsilon_{yy}^{lim}|$ plots for every load point. Fig 4.4a and 4.4b yields these curves for CG and FG samples, respectively. The character of these CDFs are similar over both samples.

There were two reasons to provide V vs. $|\varepsilon_{yy}^{lim}|$ plots. First, is to try to catch a feature on the curves that can be construed as the $|\varepsilon_{yy}^{lim}|$ value that separates dormant and twinned strain points. Second is to provide the comprehensive plots in this regard to the reader. If, in future work, $|\varepsilon_{yy}^{lim}|$ is externally introduced, the reader can look up dormant/twinned volume fractions from these plots.

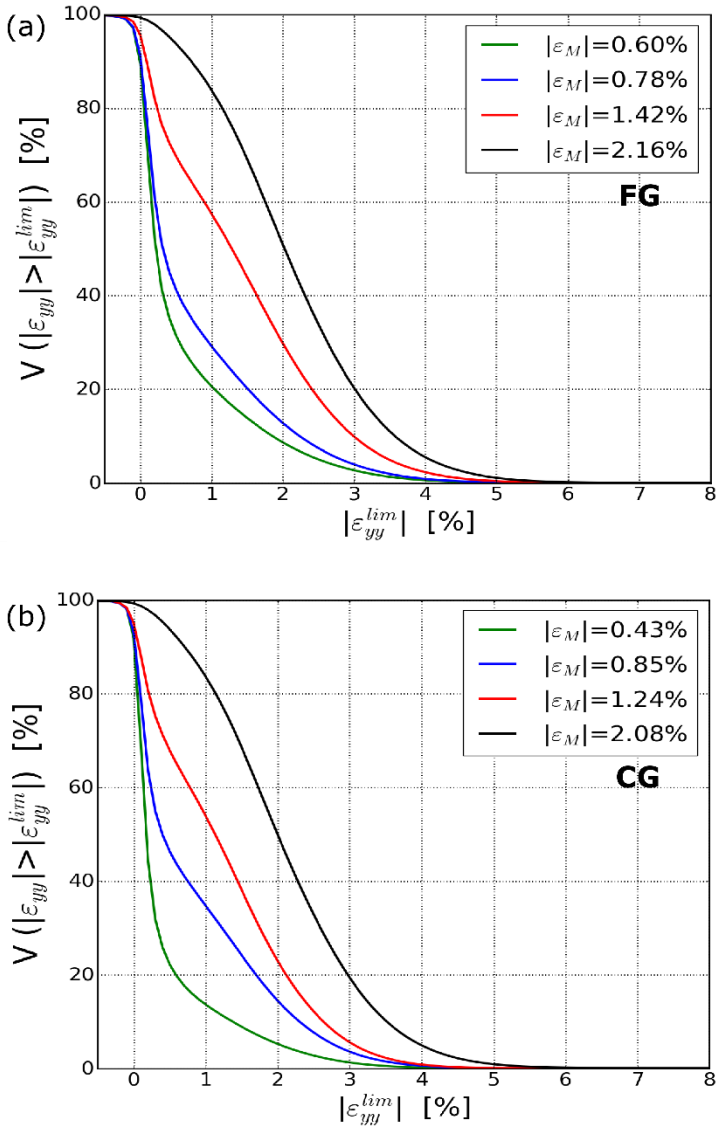

Figure 4.4 Fraction (V) of the number of filtered strain data points, ($|\varepsilon_{yy}| > |\varepsilon_{yy}^{lim}|$), to the number of the entire strain data, plotted against $|\varepsilon_{yy}^{lim}|$ for FG (a) and CG (b) at different load points.

Unfortunately, though there are certain transition features over these CDFs, there is nothing that is striking that separates high and low strain points. This is likely to be expected since the PDFs (strain histograms) did not reveal, e.g., a double peak character and the contribution of dormant points, spread out by the DIC noise overlaps with the signal of high strain points. A primary reason that the high-strain signals are also smeared is that twinning

operates at a lower length scale than the micro-DIC measurement scale, here. Averaging the strain data over DIC subsets (~12 μm) smears the localized principal twin-transformation strain (nominal 6.5%). Thus, data filtering cannot detect the boundary between dormant and deformed regions and provide critical fraction value that represents the contribution of twinning to the deformation.

5. CONCLUSION

Twin-dominant deformation in rolled Magnesium AZ31 is studied with multi-scale in situ digital image correlation (DIC) considering two different grain sizes. The samples are compressed in the loading direction that favors the activation of tensile twinning system $\{10\bar{1}2\}\langle\bar{1}011\rangle$. Both fine-grained (FG) and coarse-grained (CG) samples display intense strain localization in the form of $\pm 45°$ inclined bands. In this thesis, for the first time, the deformation band data has been geometrically filtered for standalone statistical analysis over the quantitative microscopic DIC results. The nominal average standalone band strain in the axial direction has been found to span from 1.5 to 2 %. Average strain is found nearly zero outside the deformation bands (dormant regions, see Figure3.6a). This confirms that strain is accommodated by the bands where tensile twinning is the dominant deformation mechanism. It has been documented that the localized deformation in the bands stem from collaborative tensile twinning [21], but since the strain content of the bands is well below the twin transformation strain (6.5%), these macroscopic band structures clearly do not undergo complete twin transformation. Indeed, the ratio of the average band strain to the characteristic twin transformation strain presents a measure for twin volume fraction inside the deformation bands. This measure can provide a reasonable approximation of the actual twin volume fraction (inside the bands) when no other plastic deformation micro-mechanisms (basal slip, etc.) are operational to any substantial degree. For this reason, this volume fraction measure is defined as the sole-twin-activity volume fraction ,V_{STA}, in this thesis. V_{STA} is slightly higher in the deformation bands of the FG sample compared to those of the CG sample by a ~10% margin. V_{STA} remains constant for a singular band even when it expands, confirming the conjecture that band strain and corresponding V_{STA} are characteristic values. Only when bands intersect and interact, the strain in these localization structures rise noticeably. The V_{STA} values inside the (deformation bands), ranging between 24-30% imply that 70-76% of the band volume remain locally dormant domains. In an attempt to distinguish these regions inside the bands, strain maps are filtered with threshold strain values. In this approach, strains higher than a certain value are to be interpreted as candidate regions of twin activity inside the bands. However, as monolithic strain histograms of the strain data over the bands indicate, there is no clear threshold value

separating twinned and untwinned localities. An important factor is that strain data is naturally averaged over micro-DIC subsets (of 12 μm size) and smeared, mixing the signal of both dormant and twinned domains. To circumvent this ambiguity, volume fractions with any threshold strain value is plotted in the form of cumulative probability distributions in the thesis.

6. FUTURE WORK

In this thesis, grain size effect of collaborative twin-mediated deformation is studied on the rolled samples. Using the statistical analyses techniques laid out in this thesis, samples with other textures (e.g. extrusion texture) can be comparatively analyzed. This will lead to a more comprehensive understanding of the microstructural effects, including grain size and texture.

The fraction of twin-related localizations through threshold-value filtering of strain data did not succeed with the DIC parameters adopted in this thesis. Conducting in situ DIC experiments at a lower length-scale (than $0.2\ \mu m/pixel$) that is closer to twin-scale might enhance the strain data in terms of localization details. More clearly, strain histograms can then split up into peaks of dormant and twinned zones. This requires capability to use smaller subset sizes and/or using higher magnification optics.

In the future, the study in this thesis can significantly benefit from external measurements of twinned volume fraction inside the deformation bands, which was estimated with a strain ratio in this thesis. Such measurements would confirm/disconfirm the assumption that the posed sole-twin-activity volume fraction approximates actual twin volume fractions. Particularly, post-mortem, high-resolution electron-back-scatter diffraction (EBSD) measurements would be desirable; but also, high quality post mortem metallography linked to a twin-band detection software can be sufficient. In the latter, polishing and etching would be performed after the experiment and since the macroscopic bands are 2-D structures extruded into the sample, losing the exact layer of grains would not matter. If etching can lay out twinned bands and an image processing interface can auto-detect these than actual twin volume fraction could be determined.

REFERENCES

1. D. W. Brown, S. R. Agnew, M. A. M. Bourke, T. M. Holden, S. C. Vogel, and C. N. Tomé, “Internal strain and texture evolution during deformation twinning in magnesium,” *Mater. Sci. Eng. A*, vol. 399, no. 1–2, pp. 1–12, 2005.

2. M. R. Barnett, “Twinning and the ductility of magnesium alloys. Part I: ‘Tension’ twins,” *Mater. Sci. Eng. A*, vol. 464, no. 1–2, pp. 1–7, 2007.

3. S. L. Couling, J. F. Pashak, and L. Sturkey, “Unique Deformation and Aging Characteristics of Ceratin Magnesium-Base Alloys.” pp. 94–107, 1959.

4. H. Wang, B. Raeisinia, P. D. Wu, S. R. Agnew, and C. N. Tomé, “Evaluation of self-consistent polycrystal plasticity models for magnesium alloy AZ31B sheet,” *Int. J. Solids Struct.*, vol. 47, no. 21, pp. 2905–2917, 2010.

5. J. Zhang, Q. Yu, Y. Jiang, and Q. Li, “An experimental study of cyclic deformation of extruded AZ61A magnesium alloy,” *Int. J. Plast.*, vol. 27, no. 5, pp. 768–787, 2011.

6. Q. Li, Q. Yu, J. Zhang, and Y. Jiang, “Effect of strain amplitude on tension-compression fatigue behavior of extruded Mg6Al1ZnA magnesium alloy,” *Scr. Mater.*, vol. 62, no. 10, pp. 778–781, 2010.

7. R. W. Hertzberg, *Deformation and Fracture Mechanics of Engineering Materials*, 4th ed. New York: J. Wiley & Sons, 1996.

8. M. A. Meyers, O. Vöhringer, and V. A. Lubarda, “The onset of twinning in metals: A constitutive description,” *Acta Mater.*, vol. 49, no. 19, pp. 4025–4039, 2001.

9. M. R. Barnett, “A rationale for the strong dependence of mechanical twinning on

grain size," *Scr. Mater.*, vol. 59, no. 7, pp. 696–698, 2008.

10. N. Ecob and B. Ralph, "The effect of grain size on deformation twinning in a textured zinc alloy," *J. Mater. Sci.*, vol. 18, no. 8, pp. 2419–2429, 1983.

11. K. Hazeli, J. Cuadra, P. A. Vanniamparambil, and A. Kontsos, "In situ identification of twin-related bands near yielding in a magnesium alloy," *Scr. Mater.*, vol. 68, no. 1, pp. 83–86, 2013.

12. M. R. Barnett, M. D. Nave, and A. Ghaderi, "Yield point elongation due to twinning in a magnesium alloy," *Acta Mater.*, vol. 60, no. 4, pp. 1433–1443, 2012.

13. A. Ghaderi and M. R. Barnett, "Sensitivity of deformation twinning to grain size in titanium and magnesium," *Acta Mater.*, vol. 59, no. 20, pp. 7824–7839, 2011.

14. O. Muránsky, M. R. Barnett, D. G. Carr, S. C. Vogel, and E. C. Oliver, "Investigation of deformation twinning in a fine-grained and coarse-grained ZM20 Mg alloy: Combined in situ neutron diffraction and acoustic emission," *Acta Mater.*, vol. 58, no. 5, pp. 1503–1517, 2010.

15. O. Muránsky, M. R. Barnett, V. Luzin, and S. Vogel, "On the correlation between deformation twinning and Lüders-like deformation in an extruded Mg alloy: In situ neutron diffraction and EPSC.4 modelling," *Mater. Sci. Eng. A*, vol. 527, no. 6, pp. 1383–1394, 2010.

16. I. J. Beyerlein, L. Capolungo, P. E. Marshall, R. J. McCabe, and C. N. Tomé, "Statistical analyses of deformation twinning in magnesium," *Philos. Mag.*, vol. 90, no. 16, pp. 2161–2190, 2010.

17. M. A. Sutton, J. J. Orteu, and H. W. Schreier, *Image correlation in mage Correlation for Shape, Motion and Deformation Measurements: Basic Concepts,Theory and Applications*. New York, NY: Springer, 2010.

18. C. Efstathiou, H. Sehitoglu, and J. Lambros, “Multiscale strain measurements of plastically deforming polycrystalline titanium: Role of deformation heterogeneities,” *Int. J. Plast.*, vol. 26, no. 1, pp. 93–106, 2010.

19. C. Efstathiou and H. Sehitoglu, “Strain hardening and heterogeneous deformation during twinning in Hadfield steel,” *Acta Mater.*, vol. 58, no. 5, pp. 1479–1488, 2010.

20. E. Kapan, N. Shafaghi, S. Uçar, and C. C. Aydıner, “Texture-dependent character of strain heterogeneity in Magnesium AZ31 under reversed loading,” *Mater. Sci. Eng. A*, vol. 684, no. August 2016, pp. 706–711, 2017.

21. C. C. Aydiner and M. A. Telemez, “Multiscale deformation heterogeneity in twinning magnesium investigated with in situ image correlation,” *Int. J. Plast.*, vol. 56, pp. 203–218, 2014.

22. W. F. Hosford, *Mechanical behavior of materials*, 2nd ed. Cambridge: Cambridge University Press, 2009.

23. S. R. Agnew and Ö. Duygulu, “Plastic anisotropy and the role of non-basal slip in magnesium alloy AZ31B,” *Int. J. Plast.*, vol. 21, no. 6, pp. 1161–1193, Jun. 2005.

24. J. W. Christian and S. Mahajan, “Deformation twinning,” *Prog. Mater. Sci.*, vol. 39, no. 1–2, pp. 1–157, 1995.

25. M. H. Yoo, “Slip, twinning, and fracture in hexagonal close-packed metals,” *Metall. Trans. A*, vol. 12, no. 3, pp. 409–418, 1981.

26. D. H. Kim, M. V. Manuel, F. Ebrahimi, J. S. Tulenko, and S. R. Phillpot, “Deformation processes in [112??0]-textured nanocrystalline Mg by molecular dynamics simulation,” *Acta Mater.*, vol. 58, no. 19, pp. 6217–6229, 2010.

27. M. S. & C. P. C. Tsai, “Grain size effect on deformation twinning and detwinning,” *Mater. Sci. Technol.*, vol. 29, no. 6, 2013.

28. L. Capolungo, P. E. Marshall, R. J. McCabe, I. J. Beyerlein, and C. N. Tomé, “Nucleation and growth of twins in Zr: A statistical study,” *Acta Mater.*, vol. 57, no. 20, pp. 6047–6056, 2009.

29. L. Jiang, J. J. Jonas, A. A. Luo, A. K. Sachdev, and S. Godet, “Influence of {10-12} extension twinning on the flow behavior of AZ31 Mg alloy,” *Mater. Sci. Eng. A*, vol. 445–446, pp. 302–309, 2007.

30. A. Jain and S. R. Agnew, “Modeling the temperature dependent effect of twinning on the behavior of magnesium alloy AZ31B sheet,” *Mater. Sci. Eng. A*, vol. 462, no. 1–2, pp. 29–36, 2007.

31. Y. B. Chun and C. H. J. Davies, “Negative lateral strain ratio induced by deformation twinning in magnesium alloy AZ31,” *Mater. Sci. Eng. A*, vol. 528, no. 15, pp. 4941–4946, 2011.

32. B. Clausen, C. N. Tomé, D. W. Brown, and S. R. Agnew, “Reorientation and stress relaxation due to twinning: Modeling and experimental characterization for Mg,” *Acta Mater.*, vol. 56, no. 11, pp. 2456–2468, 2008.

33. D. Lecompte *et al.*, “Quality assessment of speckle patterns for digital image correlation,” *Opt. Lasers Eng.*, vol. 44, no. 11, pp. 1132–1145, 2006.

34. M. R. Barnett, M. D. Nave, and C. J. Bettles, “Deformation microstructures and textures of some cold rolled Mg alloys,” *Mater. Sci. Eng. A*, vol. 386, no. 1–2, pp. 205–211, 2004.

35. M. R. Barnett, A. Ghaderi, and J. D. Robson, “Contribution of twinning to low strain deformation in a Mg alloy,” *Metall. Mater. Trans. A Phys. Metall. Mater. Sci.*, vol.

45, no. 8, pp. 3213–3221, 2013.

APPENDIX A: POLE FIGURES

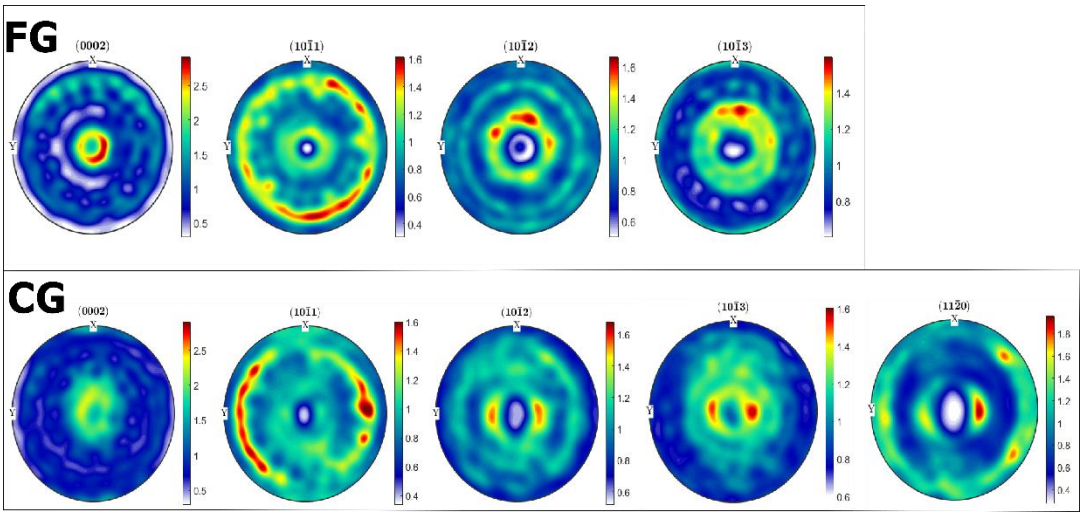

Figure A.1. Pole Figures of FG and CG materials obtained from a Bruker D8 Discover X-Ray Diffraction System